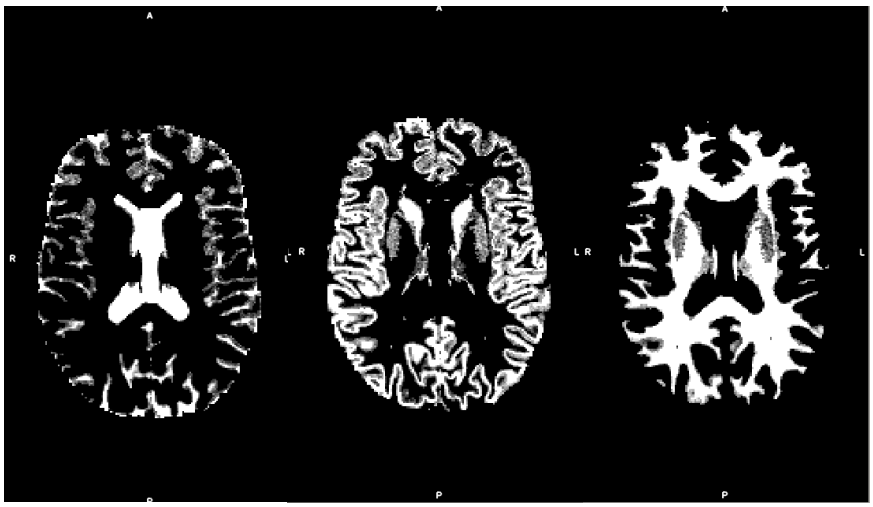

Comparison of Brain Perfusion Parameters in Hypocapnia and Normocapnia Using Multi-PLD Arterial Spin Labeling MRI

Wai Teng Liu
Medical Physics
Department of Physics and Astronomy
2019

Supervisor
Patrícia Margarida Piedade Figueiredo, Assistant Professor
Instituto Superior Técnico

U.PORTO

FACULDADE DE CIÊNCIAS
UNIVERSIDADE DO PORTO

Todas as correções determinadas pelo júri, e só essas, foram efetuadas.
O Presidente do Júri,

Porto, _____/_____/_____

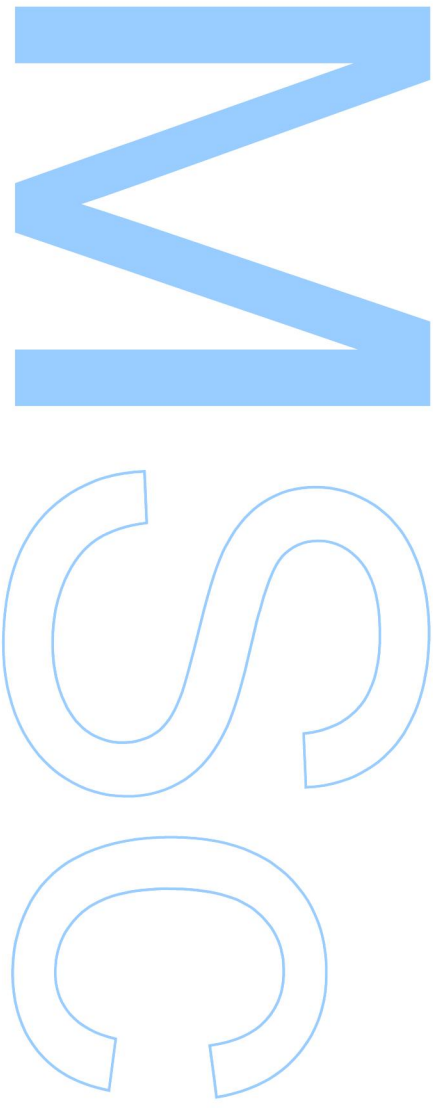

ABSTRACT

In this work, a non-invasive quantitative imaging technique for measuring brain perfusion parameters is presented, using multi-post labeling delay Arterial Spin Labelling (ASL) MRI. The objective of this work was to compare the brain perfusion parameters such as cerebral blood flow (CBF), arterial transit time (ATT), and arterial blood volume (aBV) between the condition of hypocapnia and normocapnia, and also to compare different calibration methods to compute the absolute CBF and aBV.

ASL data were acquired using a 3T MRI scanner using the PICORE-Q2TIPS sequence on 13 heathy subjects. During the acquisition, all the subjects were asked to perform two breathing tasks: the normal breathing and paced deep breathing, to achieve normocapnia and hypocapnia, respectively. The end-tidal carbon dioxide pressure ($P_{ET}CO_2$) of each subject was recorded simultaneously with the breathing tasks.

All the ASL and structural image data were processed using FMRIB Software Library (FSL) tool and Bayesian Inference for Arterial Spin Labelling (BASIL). In this stage, the processing steps included brain extraction, segmentation, registration, motion correction, masking, model fitting and calibration. For the calibration step, different types of calibration methods were compared using saturation recovery, including reference tissue-based method with and without fixed saturation efficiency, as well as voxel-wise-based method with and without fixed saturation efficiency.

The parameter maps of CBF, ATT, and aBV were obtained from the mentioned processing steps above. A grey matter mask was used to perform ROI comparison. A voxel-wise comparison was executed using Threshold-Free Cluster Enhancement to perform a statistical analysis of all parameter maps in the condition of hypocapnia and normocapnia. The calibration methods were compared using one-way ANOVA. There was no significant difference between normo- and hypocapnia condition within each subject and the group mean. The comparison of calibration methods indicated a significant difference between the methods using reference tissue cerebral spinal fluid and the others.

In conclusion, the quantification of brain perfusion parameters and comparison of calibration methods were achieved successfully, having a significant difference between calibration methods. However, no significant difference between hypocapnia and normocapnia was found in this work.

Key words: Magnetic Resonance Imaging, Arterial Spin Labelling, Hypocapnia, Brain perfusion parameter, Paced Deep Breathing

RESUMO

Neste trabalho realizou-se uma análise de métodos de imagiologia quantitativa não invasiva para estimação de parâmetros de perfusão cerebral, sob condições de hipocapnia e normocapnia, utilizando *arterial spin labelling* (ASL) em ressonância magnética. O objectivo deste trabalho foi comparar parâmetros de perfusão como *CBF, ATT e aBV* entre as condições de hipocapnia e normocapnia, tal como comparar diferentes métodos de calibração para estimar/calcular a *aBV e o* valor absoluto de *CBF*.

Os dados de ASL foram adquiridos com um scanner de RM de 3T usando a sequência de aquisição PICORE-Q2TIPS em 13 sujeitos saudáveis. Durante a aquisição os sujeitos tinham que realizar duas tarefas de respiração: uma de respiração normal, outra de respiração profunda e lenta, de forma a induzir estados de normocapnia e hipocapnia, respectivamente. A pressão-final de dióxido de carbono ($P_{ET}CO_2$) foi gravada em simultâneo com as tarefas de respiração.

Os dados de ASL e imagens de RM estructural foram processados com FSL e BASIL. Nesta parte do processamento os passos foram a extracção do cérebro, segmentação, registos, correção de movimento, criação de máscarás anatómicas binárias, *fitting* de modelos e calibração. No passo de calibração, foram comparados diferentes métodos de calibração utilizando *saturation recovery*, incluindo métodos *tissue-based* com e sem eficiência de saturação fixa, e também métodos voxel-wise com e sem eficiência de saturação fixa.

Os mapas de parâmetros de CBF, ATT e aBV foram obtidos através dos passos supramencionados. Definiu-se uma máscara de matéria cinzenta para realizar uma análise comparativa de regiões de interesse. Foi realiza uma comparação *voxel-wise* utilizando *Threshold-Free Cluster Enhancement* para realizar análise estatística de todos os mapas de parâmetros nas condições de hipocapnia e normocapnia. Os métodos de calibração foram comparados com tests *one-way ANOVA*. Não houve significância estatística entre cada sujeito e a média do grupo. A comparação de diferentes métodos de calibração sugere significância estatística significativa entre os métodos. Concluindo, a quantificação de parâmetros de perfusão e comparação de métodos foi realizada. Contudo, não houve significância estatística entre as condições de hipocapnia e normocapnia.

Palavras chave: Imagiologia por Ressonância Magnética, *Arterial Spin Labelling*, Hipocapnia, parâmetros de perfusão cerebral, respiração profunda

ACKNOWLEDGEMENT

I would first like to thank my supervisor Professor Patrícia Figueiredo for the opportunity of developing my master's thesis and learning in Laseeb, and also for her guidance and advise in this work.

A special thanks to Joana Pinto for her great helping when I was falling into a problem and had a question about my work. I would also thank Francisco Azevedo for his helping in Portuguese abstract and his opinion for my thesis.

To all my colleagues in Laseeb and FCUP who provided opinion and help when I needed.

Finally, I must express my very profound gratitude to my parents and to my girlfriend for their support and continuous encouragement throughout my years of study and writing this thesis. This accomplishment would not have been possible without them. Thank you.

TABLE OF CONTENTS

LIST OF ACRONYM AND ABBREVIATION

ATT	–	Arterial Arrival Time
aBV	–	Arterial Blood Volume
ARD	–	Automatic Relevance Determination
ASL	–	Arterial Spin Labelling
BASIL	–	Bayesian Inference for Arterial Spin Labelling MRI
BAT	–	Blood Arrival Time
CASL	–	Continuous Arterial Spine Labelling
CBF	–	Cerebral Blood Flow
CBV	–	Cerebral Blood Volume
CPP	–	Cerebral Perfusion pressure
CSF	–	Cerebral Spinal Fluid
CT	–	Computed Tomography
CVR	–	Cerebral Vascular Reactivity
CVRe	–	Cerebral Vascular Resistance
DCE	–	Dynamic Contrast Enhancement
DSC	–	Dynamic Susceptibility Contrast
EPI	–	Echo Planar Imaging
EPISTAR	–	Echo Planar Imaging-based Signal Targeting by Alternating Radiofrequency Pulses
FAIR	–	Flow-sensitive Alternating Inversion Recovery
FAST	–	FMRIB's Automated Segmentation Tool
FLIRT	–	FMRIB's Linear Registration Tool
fMRI	–	Functional Magnetic Resonance Imaging
FSL	–	FIMRIB Software Library
GLM	–	General Linear Model
GM	–	Grey Matter
LSQ	–	Least Squares methods
MPRAGE	–	Magnetisation-Prepared Rapid Acquisition with Gradient Echo
MRI	–	Magnetic Resonance Imaging
PASL	–	Pulsed Arterial Spin Labelling
PC-MRI	–	Phase Contrast Magnetic Resonance Imaging
PCASL	–	Pseudo-Continuous Arterial Spin Labelling

PDB	–	Paced Deep Breathing
PET	–	Positron Emission Tomography
$P_{ET}CO_2$	–	End-Tidal CO_2 pressure
PICORE	–	Proximal Inversion with a Control for Off-Resonance Effects
PLD	–	Post Labelling Delay
Q2TIPS	–	QUIPPS II with Thin-slice TI_1 Periodic Saturation
QUIPPS	–	Quantitative Imaging of Perfusion using a Single Subtraction
RF	–	Radio-frequency
SNR	–	Signal to Noise Ratio
SPECT	–	Single Photon Emission Computed Tomography
TE	–	Echo Time
TFCE	–	Threshold-Free Cluster Enhancement
TI	–	Inversion Time
TR	–	Repetition Time
vBV	–	Venous Blood Volume
WM	–	White Matter

1. INTRODUCTION

1.1 Brain perfusion parameters

The perfusion in human body, is usually defined as the process of delivery of nutrients, oxygen and others biological substances through the passage of arterial blood (Günther, 2013). Particularly, the brain perfusion is referred as cerebral blood flow (CBF) when accessing the behaviour of arterial blood in brain. The brain perfusion is a critical index for evaluating the functions of brain and cerebral vasculature. Therefore, the quantification of perfusion is necessary for clinical diagnosis and predicting the condition of patients. In this section, the brain perfusion parameters and their relationships are described.

The CBF is usually measured in millilitres per 100 grams of tissue per minute (ml/100g/min) (Buxton, 2002). The quantity of CBF in time is differs in different individuals, different size of artery, even the same artery but under different conditions. The CBF is directly associated with the cerebral perfusion pressure (CPP), which is the pressure that causes the arterial blood flowing into brain. By dividing CPP with cerebral vascular resistance (CVRe), the relationships of them is given by (Gomes, 2015; Pinto, 2012):

$$CBF = \frac{CPP}{CVRe} \tag{1.1}$$

Furthermore, how fast does the arterial blood flow within the brain or how long does it take to flow into a specific tissue is also a factor that needs to be concerned. The arterial transit time (ATT), is a specific parameter in arterial spin labelling MRI, it indicates the time duration that the arterial blood reach to the tissue from the tagging region. This parameter can offer an additional measured in the characterization of hypoperfusion due to cerebrovascular disease (MacIntosh et al., 2010; Bokkers et al., 2008). Nevertheless, some previous studies presented that the ATT varies due to the neuronal activation (MacIntosh et al., 2010; Francis et al., 2008; Hendrikse et al. 2003; Yang et al., 2000) or as the consequence of the vascular reactivity challenge (MacIntosh et al., 2010; MacIntosh et al., 2008; Hendrikse et al., 2008) in healthy individuals.

On the other hand, the arterial blood volume (aBV) is also a parameter that needs to be considered when discussing the brain perfusion parameters. It is defined as the amount of volume of the arterial blood that can fill the capacity of arterial cerebral vasculature (Hua et al., 2019). In the previous study presented by J. Hua et al. in 2019, they defined the aBV can be

considered as one of the compartments that contributes to the total cerebral volume, the relationships between them is given by (Hua et al., 2019):

$$CBV = aBV + vBV \tag{1.2}$$

The expression above assumes that the total cerebral blood volume is composed by the compartment of aBV and vBV, since the physiological and functional roles of arterial and venous blood vessels are different, and therefore the different flow-volume coupling (Hua et al., 2019). Moreover, the total cerebral blood volume CBV can also be related to CBF by the power law relationship (Grub et al., 1974):

$$CBV = 0.80 \times CBF^{0.38} \tag{1.3}$$

This relationship was concluded from a study of anesthetized rhesus monkeys. However, this relationship may differ with many factors, such as species, brain region, stimulus type, strength, and many other of them (Hua et al. 2019; Kida et al., 2007; Rostrup et al., 2005; Wu etal., 2002). Nevertheless, the relationships between CBF and CBV, aBV, vBV were still reported based on the equation (1.3) by several human studies of MRI with using different type of stimulation. (Hua et al., 2019; Hua et al., 2011; Hua et al., 2010; Chen and Pike, 2010; Chen and Pike, 2009).

After a brief introduction of CBF, ATT, and aBV, the cerebrovascular reactivity (CVR) should also be discussed when talking about the behaviour of CBF and aBV, since the changes of those parameters are related to the changes in CVR (Liu et al. 2019). In general, CVR can be divided in two aspects: vasoconstriction and vasodilation. In the former, the arterial vessels are constricted, causing the increase of CPP and thus the increase of CVRe. In the latter, the arterial vessels are dilated, causing the decrease of CPP and therefore the decrease of CVRe (Cipolla, 2009). Therefore, the constriction or dilation of arterial vasculature can result in the alteration of CBF, aBV and ATT (Derdeyn et al., 2002; Lee and Kim, 2017).

1.2 Hypocapnia

In order to investigate the CVR of arterial cerebral vessel in heathy individual through the brain perfusion parameters such as CBF, aBV, and ATT, the manner to induce the vasoconstriction and vasodilation should be considered properly. In the previous studies that related to the investigation of CVR, they were applied frequently the induced-hypercapnia or hypocapnia by

breathing task or CO_2 inhalation for this purpose. In this section, the condition of hypocapnia will be focused only, since this work aimed to induce hypocapnia to access the brain perfusion.

Hypocapnia is defined as the decrease in alveolar and blood carbon dioxide (CO_2) levels below the normal reference range of 35 mm Hg. As the CO_2 level decreases in alveolar, causing the decrease of intravascular PCO_2 and the resultant increase of perivascular and intraneuronal pH, inducing vasoconstriction, and therefore the reduction of CBF (Posse et al., 1997). While the level of CO_2 decreases, the level of O_2 increases at the same time because of the increase of perivascular and intraneuronal pH. Hypocapnia can be achieved by hyperventilation of the testing individuals, in which the rhythm of breathing of testing individuals can be instructed visually or audibly.

Hyperventilation breathing protocol was applied to induce vasoconstriction and hypocapnia in the previous presented studies (Krainik et al., 2005; Mäkiranta et al., 2004; Weckesser et al., 1999; Posse et al., 1997). In this manner, consisting a prolonged period of fast and deep unpaced breathing, it may cause some undesired effects such as dizziness, numbness or limb paraesthesia, and those effects are prone to motion artefact (Sousa et al., 2014). Alternatively, a controlled hyperventilation breathing protocol called Paced Deep Breathing (PDB) was proposed, by applying the paced breathing to increase the respiratory rate, depth over short periods of time and alternated with normal breathing (Vogt et al., 2011; Bright et al., 2009; Birn et al., 2008).

In the manner of PDB, it is usually performed by alternating deep breathing with normal breathing in a certain duration. For example, in the previous study presented by Sousa et al. in 2014, the testing individuals were told to breathe freely in the initial stage in order to establish a baseline, then they were asked to breathe deeply when paced for 40s during PDB and follow by a free breathing period again for 60s, the period of PDB and free breathing were repeated 2 times for each individual, having the total duration of breathing task of 3 minutes and 45 seconds. This way, the condition of mild hypocapnia and the resultant vasoconstriction were achieved (Sousa et al., 2014).

1.3 Imaging techniques for estimation of brain perfusion

To investigate or evaluate the brain perfusion, there are several medical imaging modalities available. In this section, different methods for investigating the brain perfusion are revealed briefly.

1.31 Computed Tomography

Computed Tomography (CT) is one of the most common imaging modalities nowadays. It is characterized by short scanning time with the image of high-resolution anatomical structure, it is possible to access human brain in a short period of time and having an acceptable result for diagnosis purpose. However, the main disadvantages of CT are the relative high dose of radiation exposure than others and the poor soft tissue contrast, especially in the brain tissue. In the perspective of measuring the CBF using CT, one of the most common CBF tracer is Xenon 133 gas, which can be mixed with oxygen and inhaled via the respiratory system, and the CBF map can be obtained when the tracer gas arrives at the imaging region along with the blood flow. Few assessments of CBF using Xe-133 CT were presented in the previous studies. (Pindozla et al., 2001; Yonas et al., 1991)

1.3.2 PET and SPECT

Positron Emission Tomography (PET) is an imaging technique of nuclear medicine. By injecting the radiopharmaceutical intravenously into the circulation system of patient, the emitted photon pair of 511 KeV that are from the reaction of annihilation, can then be detected by the scanner. After receiving the photons that come out of the body, the resultant signals are reconstructed as an image. Due to the poor spatial resolution of this technique, it is usually combined with CT or MRI in one scanner and operating simultaneously, the image of PET and CT/MRI can be superposed together to have the anatomical information of the target lesion. To quantify the brain perfusion using PET, the tracer kinetic model is used for this purpose, which describes the time-varying distribution of radiopharmaceuticals in the body to calculate the flow rate of the tracer molecule and therefore the brain perfusion. A presented study used ^{15}O-labelled water and oxygen as CBF tracer (Ssali et al., 2019).

On the other hand of the imaging technique in nuclear medicine, the Single Photon Emission Computed Tomography (SPECT) is also used widely for brain perfusion. In general, the principle of its acquisition technique is similar to PET, but using different type of radiopharmaceutical that has a different mechanism of emitting energy to the detector. However, the poor spatial resolution is the main disadvantage of it, as same as PET.

1.3.3 Magnetic Resonance Imaging

The final imaging modality that discussed in this section is Magnetic Resonance Imaging (MRI), and it is also the one that was used in this work. The main advantages of MRI are the absence of ionizing radiation and the extraordinary soft tissue contrast; therefore, MRI may be the best imaging modality for the investigation of brain so far. In this imaging technique,

there are three main methods to have a perfusion-weighted image, the first one is dynamic susceptibility contrast (DSC), which utilises the magnetic field susceptibility caused by the passage of the extrinsic contrast agent, and uses dynamic T2 imaging for acquisition; the second one is dynamic contrast enhancement (DCE), it also needs extrinsic agent for dynamic T1 imaging (Alsaedi et al, 2018).

The last one, and the one was applied in this work is arterial spin labelling (ASL), an imaging technique without the use of extrinsic contrast agent. It is a completely non-invasive imaging technique that uses arterial blood as a contrast agent, particularly for the assessment of brain perfusion. In the absence of contrast agent, ASL has the potential to be used widely for the patient who has allergy of contrast agent or poor renal function for the clearance of the contrast agent. Furthermore, this imaging technique is not only for brain perfusion, but also has the potential to be used for the angiography of brain and the other parts of human body, since it uses the arterial blood as the contrast agent, and the majority of the large artery can be used as the source of tracer such as the aorta (Jezzard et al., 2018; Aherne et al., 2019), but it is out of the scope of this work. More details about the principles of MRI and the techniques of ASL are described in the next chapter.

1.4 Motivation

By giving the importance of brain perfusion parameters, their relationships, and how they behave in different concentration level of intravascular gas, the motivation of this work becomes clearer and more explainable. As mentioned in the very beginning, the brain perfusion is a process of transferring substances such as oxygen, nutrients, hormones that we need, also, washing out the wastes and toxicity from the circulation system, like CO_2 and other useless products from the metabolism, and therefore it plays a critical role in our body.

Although the circulation system has an auto-regulation to control the perfusion, balances the concentration of different substance and regulates the condition of organs, the intravascular perfusion is still possible to be problematic when meeting a dysfunction because of disease, leading a further disorder of organs, especially in our brain.

For instance, the aBV may be an important microvascular parameter to monitor arterial steno-occlusive disease in the brain, and it can be affected by cervical and intracranial arterial stenosis (Donahue et al., 2017). In the early stage of the disease, it presents a decrease in cerebral perfusion pressure, resulting in the increase of aBV due the arterial vessel is dilated by the auto-regulatory response of the arterial vasculature in order to maintain CBF (Derdeyn et

al., 2002). In the aspect of ATT, in the presented study of hypertension by Lee and Kim in 2017, reported that the arterial transit time was prolonged in the hypertensive group compared with the control group, in which the CBF were similar in both groups.

In the case of brain tumour, it presented the abnormal total CBV in the region of tumour due to angiogenesis, which is a critical step of tumour growth (Folkman, 1995), results in altered number of blood vessels. Therefore, the measure of tumour presented the essential diagnostic value for predicting the tumour grade and the response to therapeutics (Law et al., 2004). Moreover, the tumour aBV may be the more specific measure for tumour perfusion (Hua et al., 2019), because of the arterioles may be generated by the process of angiogenesis during the tumour growth (Hansen-Smith et al., 2001).

Therefore, it is necessary to investigate and study the brain perfusion parameters comprehensively in order to have a whole picture of their mechanism, how they behave under different condition, making a connection between them and giving their information as the reference to the medical professionals for the diagnosis purpose. In the further sections, several imaging techniques that are able to access the brain parameters are discussed, including the one was used in this work, the arterial spin labelling MRI.

1.5 State of the art

In this section, a brief review of brain perfusion assessment using arterial spin labelling MRI within the condition of hypocapnia, normocapnia, and hypercapnia is presented. Although hypercapnia was not the main topic of this work, its mechanism and consequences are opposite to hypocapnia, thus, it is better to review both of them for having a comprehensive insight.

Regarding the quantification of CBF, ATT, and aBV using arterial spin labelling MRI, Sousa et al. presented a study in terms of the reproducibility of quantification using multiple post-labelling delay arterial spin labelling with PICORE-Q2TIPS sequence. This study aimed to 3 aspects mainly: to assess the reproducibility of quantification in global perfusion and regional pattern of CBF, ATT, and aBV with nonflow-suppression and macroflow-suppression; to compare the estimated perfusion parameters from different models (LSQ and BASIL); to compare the estimated aBV from model-free and model-based manner (Sousa et al., 2014).

Among the results that presented by Sousa et al., there were no significant differences between the estimated CBF from both models and obtained a reproducible result. However, a significant interaction between flow-suppression and estimated methods was found in ATT. In

the aspect of aBV, estimates from BASIL was considerably higher than the one from LSQ and the reproducible estimates were also achieved. In conclusion, the reproducible estimates were accomplished for CBF, ATT, and aBV in both estimation model with low inter-subject variability.

For research on hypercapnia, Nöth et al. presented a study of cerebral vascular response to hypercapnia in comparison with normocapnia using PASL under 1.5T and 3T magnetic field, they reported that the mean CBF in grey matter of a group of 9 subjects under hypercapnia was significantly higher than the one in normocapnia. However, the results had no significant difference between 1.5T and 3T magnetic field (Nöth et al., 2006).

Another study of hypercapnia in human brainstem cerebrovascular function presented by Warnert et al. in 2014, the CBF, ATT, and aBV were obtained successfully from the whole brainstem, gray matter, cerebellum, and occipital pole using multi-inversion time PASL in hypercapnia and normocapnia. This study reported that the CBF and aBV increased significantly both in the region of cerebellum, gray matter, and occipital pole during hypercapnia in comparison with normocapnia (Warnert et al., 2014). In the same year, Donachue et al. also reported that CBF and BAT were higher and shorter in hypercapnia than the one in normocapnia, respectively (Donachue et al., 2014).

One thing should be mentioned that the research on quantification of CBF, ATT and aBV in hypocapnia using arterial spin labelling MRI were not reported very much, most of researches focused on hypercapnia only or utilised other technique of MRI to investigate the brain perfusion in hypocapnia. Therefore, the research field of hemodynamic in the condition of hypocapnia using ASL is worth investigating and it is also the importance of this work. Nevertheless, few previous studies for quantifying the brain perfusion parameters in hypocapnia using different imaging technique are present in the following.

Coverdale et al. presented a study of CBF quantification in middle cerebral artery during hypercapnia and hypocapnia using phase contrast MRI (PC-MRI), their results of CBF measurement in hypercapnia were in the agreement with the studies that mentioned above; in the aspect of hypocapnia, they reported that the CBF during hypocapnia was significantly lower than the one in baseline. $P_{ET}CO_2$ recording was also performed in this study. During hypocapnia, the mean value of $P_{ET}CO_2$ in 19 subjects showed a significant decrease in comparison with baseline (Coverdale et al., 2014).

A similar research on middle cerebral artery using 7T MRI was also presented by Verbree et al. In this study, investigators aimed to measure the diameter of middle cerebral artery on MR

image and tried to make a correlation between $P_{ET}CO_2$ and diameter of middle cerebral artery. Among the results, they reported that the diameter of middle cerebral artery was affected by the level of $P_{ET}CO_2$ during moderate hypercapnia, which was achieved by CO_2 inhalation with +2kPa (+15 mmHg) relative to the baseline. Nevertheless, the group mean of $P_{ET}CO_2$ within 10 subjects presented a significant increase and decrease in hyper and hypocapnia compared with the baseline, respectively (Verbree et al., 2014).

Another investigation on CBF changes in hypocapnia vs. normocapnia using DSC-MRI reported that the group mean value of CBF and $P_{ET}CO_2$ within 8 subjects significantly decreased in hypocapnia, having a relative CBF and $P_{ET}CO_2$ decreasing of 29% and 33% from normocapnia, respectively. Also, the investigation of mean transit time was performed in this study, reported that the mean transit time was increased due to the vasoconstriction during hypocapnia (Wirestam et al., 2009).

For the different imaging technique, the quantification of CBF and CBV was also reported from the studies using PET. Ito et al. presented a PET study using radiopharmaceutical of $H_2{}^{15}O$ and ^{11}CO to investigate brain perfusion in hypercapnia and hypocapnia. In the PET measurement with $H_2{}^{15}O$ and ^{11}CO, the significant increases and decreases of CBF, CBV were observed within the region of cerebral cortex and cerebellum during hypercapnia and hypocapnia compared with normocapnia, respectively. They also investigated the MTT in both conditions, reported that the MTT was shorten and prolonged significantly during hypercapnia and hypocapnia, respectively (Ito et al., 2003).

A CBF quantification study using PET/MRI was presented recently by Ssali et al., this study aimed to investigate CBF using PET with ^{15}O-water injection and PC-MRI simultaneously both in hypercapnia and hypocapnia, and to make a correlation between the result of PET and MRI. The results indicated that the CBF quantification both result from PET and MRI had a strong correlation. Moreover, the investigators also compared the result of CBF quantification separately in hypo-, normo-, and hypercapnia, and the strong correlation between CBF of PET and MRI was also found in both condition (Ssali et al., 2019).

1.6 Aim and objective

This work aimed to investigate and compare the CBF, ATT, and aBV of human brain between normocapnia and hypocapnia using multiple post-labelling delay pulsed ASL MRI. By applying paced deep breathing on each subject, the level of intravascular CO_2 was decreased and the condition of hypocapnia was accomplished.

The values of CBF and aBV were expected to be lower and the longer ATT was also expected in the condition of hypocapnia than in normocapnia, since the more the vasoconstriction, the less the arterial blood can pass through in the certain time, and therefore the longer the arterial arrival time. The use of Bayesian inference approach with general kinetic model and the processing tools in this work was not only to estimate the perfusion parameters, but also to test the capacity of current version of FSL and BASIL for analysing arterial spin labelling MRI data.

On the other hand, the methods for calibrating the CBF, aBV, and ATT maps were also tested and compared using different reference tissue and calibration mode. The purpose of calibration is to establish a standard scale of the concentration of the labelled blood, having the absolute value of CBF and aBV, achieving by estimation of the magnetization of arterial blood, the CBF and aBV can then be compared between subjects in the same units, otherwise, the values on those images remain in arbitrary unit, which determined by the scanner type. More details of calibration are presented in chapter 3. However, the calibrated value of CBF and aBV can be impacted by the use of different reference tissue and calibration mode in the calibration, therefore, the comparison of calibration methods using different calibration mode and reference such as cerebral spinal fluid, grey matter, and white matter, was one of the objectives in this work.

2. Basic principle of Magnetic Resonance Imaging and Arterial Spin Labelling MRI

2.1 Basic principle of Magnetic Resonance Imaging

In this section, the basic principles of MRI are described. In 1946, the phenomenon of nuclear magnetic resonance was introduced by two research groups, Purcell et al. and Bloch et al, respectively. This phenomenon is the main theoretical background that supports the principles of MRI. to understand the phenomenon of NMR, the first thing to explain is the nuclear spin system and how it behaves under an external magnetic field.

In general, a nuclear spin system means the ensemble of nuclei of the same type and each nucleus has its own nuclear magnetic moment if it has a non-zero spin. In the absence of the external static magnetic field, the orientation of magnetic moment of those nuclei in this nuclear spin system is distributed randomly and the whole spin system yields zero of the net magnetisations. Based on the theories of quantum mechanics, the magnitude of magnetic moment μ of each nucleus in a nuclear spin system is given by (Liang and Lauterbur, 2000):

$$\mu = \gamma\hbar\sqrt{I(I+1)} \tag{2.1}$$

where γ is a physical constant known as the *gyromagnetic ratio*, $\hbar$ is the *Planck's constant*, and I is the nuclear spin number. Basically, the nuclear spin number can be integer, half-integer, or zero. The value of I for a particular nucleus is determined by: (1) Nuclei with an odd mass number have half-integer spin. (2) Nuclei with an odd mass number and an even charge number have zero spin. (3) Nuclei with even mass number but odd charge number have integer spin. For the NMR-active nucleus, its nuclear spin number must be a non-zero value (Liang and Lauterbur, 2000). Therefore, hydrogen is usually used be the target of study in MRI, since it composes the majority of substance in our body, such as water and fat.

If a nuclear spin system is placed under an external static magnetic field, each nucleus in the spin system undergo a phenomenon called nuclear precession (figure 2.1), in which the magnetic moment of each nucleus rotates along with the axis of the external magnetic field. By assuming the magnetic moment of each nucleus in the spin system is a classical moment vector without mutual interaction, the nuclear precession can be expressed by (Liang and Lauterbur, 2000):

$$\begin{cases} \mu_{xy}(t) = \mu_{xy}(0)e^{-i\gamma B_0 t} \\ \mu_z(t) = \mu_z(0) \end{cases} \tag{2.2}$$

According to the expression above, the angular frequency of precession is:

$$\omega_0 = \gamma B_0 \tag{2.3}$$

The angular frequency of precession, or known as *Larmor frequency* is the natural resonance frequency of a spin system and it is linearly dependent with the strength of the applied magnetic field and the value of gyromagnetic ratio. An example of precession is presented in figure 2.1.

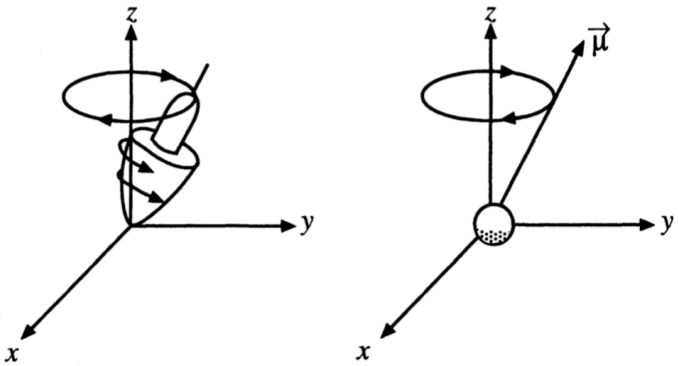

Figure 2.1: Precession of a nuclear spin (left) and its magnetic moment (right) along the z-axis of the external magnetic field. Adapted from Liang and Lauterbur, 2000.

On the other hand, during the nuclei of the nuclear spin system experience precession, their magnetic moments align with respect to the z-axis of the applied magnetic field and split in two orientations from their original orientation, one is parallel to the applied field and the other one is antiparallel to the applied field, or spin pointing up and spin pointing down, respectively. An example of this phenomenon is shown schematically in figure 2.2.

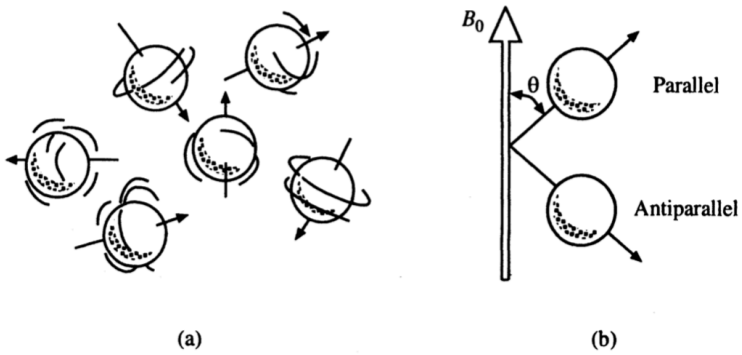

Figure 2.2: The behaviour of a spin system in natural state (a) and under an external magnetic field (b). After the application of the external field, the spins are separated in parallel and antiparallel from their original status, depending on their energy state. Adapted from Liang and Lauterbur, 2000.

As mentioned before, the magnetic moments of a nuclear spin system are distributed randomly when there is no external magnetic field. After applying an external magnetic field, the z-component of the magnetic moments become certain due to the applied field, can be expressed by (Liang and Lauterbur, 2000):

$$\mu_z = \gamma m_I \hbar \tag{2.4}$$

Where the m_I is the *magnetic quantum number*, which determines the orientation of magnetic moments that experience under the external magnetic field by taking the following set of values:

$$m_I = -I, -I+1, I \ldots 1 \tag{2.5}$$

While the longitudinal component of magnetic moment goes along with the direction of the applied field, the direction of its transverse component remains random, and also expressed by (Liang and Lauterbur, 2000):

$$\left|\overrightarrow{\mu_{xy}}\right| = \gamma\hbar\sqrt{I(I+1) - m_I^2} \tag{2.6}$$

Therefore, the orientation of magnetic moment that experiences under an external magnetic field, can be determined whether parallel or antiparallel to the direction of B_0 by the magnetic quantum number m_I. Furthermore, the energy of interaction between spins and external magnetic field is split in two energy states and can be expressed by (Liang and Lauterbur, 2000):

$$E = -\gamma m_I \hbar B_0 \tag{2.7}$$

According to the equation above, for a spin system of hydrogen, it results in two energy states for pointing up spins and pointing down spins, since the m_I of hydrogen atom is $\pm\frac{1}{2}$, having a nonzero energy difference of 5.64 x 10^{-32}, in this case. This nonzero difference in energy level between two spin states is known as the *Zeeman splitting phenomenon*.

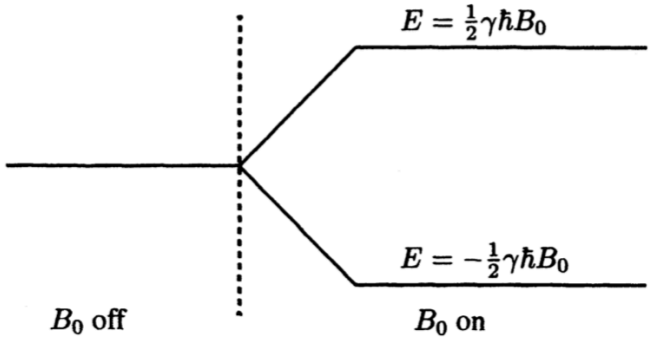

Figure 2.3: Zeeman splitting phenomenon, which describes the splitting of energy state of the spin system after applying an external magnetic field. Adapted from Liang and Lauterbur, 2000.

By calculating the nonzero energy difference between the pointing-up spins and the pointing-down spins, the number of them can then be calculated. Usually, the number of pointing-up spins is slightly greater than the number of pointing-down spins, thus, yielding a nonzero value of net magnetization for a nuclear spin system.

Through the radiofrequency pulse or called additional magnetic field B_1 with the Larmor frequency, the magnitude of the magnetic moments of z-axis in the spin system starts to reduce, the one of xy-axis starts to be focused in a certain orientation and have a net magnitude, which depends on the direction and the flip angle of the applied B_1. This way, the orientation of the net magnetization in the spin system is therefore shifted to the xy-axis from the z-axis, and this is referred to RF excitation or resonance. An example of this phenomenon is presented schematically in figure 2.4.

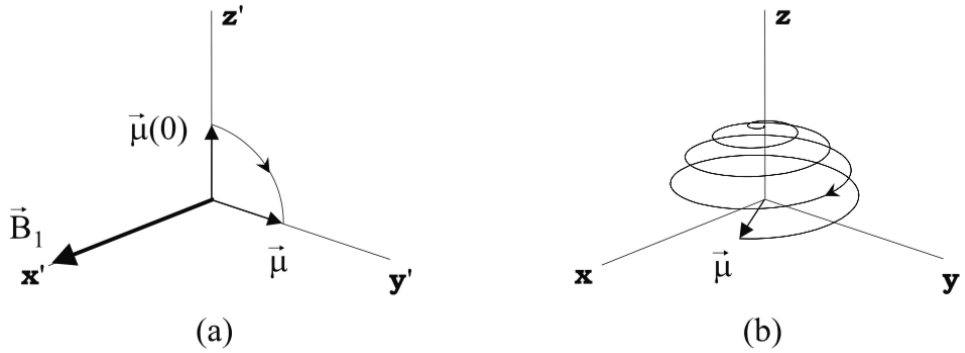

Figure 2.4: (a) presents the effect on the magnetic moment of a single spin in rotating frame after applying an additional magnetic field on x direction, the net magnetisation is shifted to the transverse plane from the longitudinal plane. (b) illustrates the same effect on the same spin in laboratory frame, showing that the magnetic moment goes spirally about the z-axis, from the longitudinal plane to the transverse plane (Brown et al., 2014).

After the excitation, the magnetization of the spin system starts to recover to its equilibrium state and undergo a phenomenon called relaxation if the additional magnetic field B_1 is no longer appear. In the absence of B_1, the relaxation process is divided in two aspect: the T1 relaxation and T2 relaxation, which describes the time required for the longitudinal magnetization recovers to 63% of its equilibrium magnetization and the transverse magnetization recovers to 37% of its equilibrium magnetization in the spin system, respectively. An example of T1 and T2 relaxation curve and the trajectory of magnetisation during relaxation are presented in figure 2.5. By measuring the relaxation time, the difference of magnetization can be detected by radiofrequency coil and an electric signal can be generated, the resultant signal can then be processed and reconstructed as an MR image through k-space and Fourier transform.

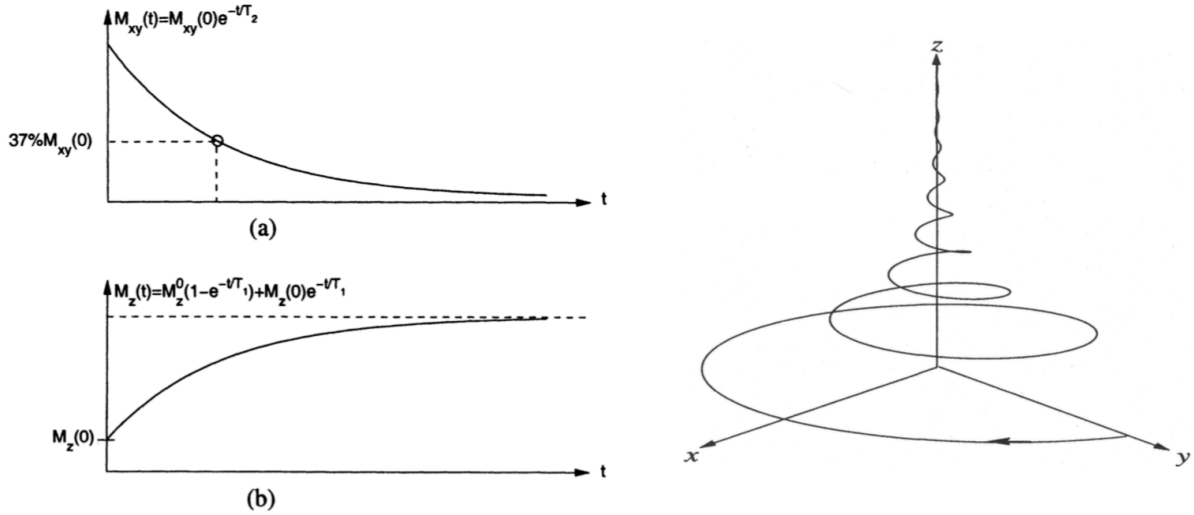

Figure 2.5: Illustration of T1 (left b) and T2 (left a) relaxation curve and the behaviour of magnetic moment during relaxation (right), Adapted from Liang and Lauterbur, 2000.

2.2 Basic principle of Arterial Spin Labelling

In the previous section, the basic principles of MRI and its signal generation were explained briefly by the perspective of the behaviour of magnetic moment and magnetisation. Now the concepts and working principles of arterial spin labelling (ASL) is easier to describe, since the main concept of this technique is to label the sample magnetically. In general, the concept of ASL is similar to the others contrast injection imaging technique, expect that, instead of injecting a contrast agent into body, this technique utilizes the arterial blood as the contrast agent to investigate the brain perfusion. In this section, the principle of ASL and the related methods for processing ASL data are revealed.

2.2.1 Image acquisition

Basically, the technique of ASL is divided in two acquisition stage mainly. In the first stage of acquisition, the first thing to do is to determine the source of tracer that consists of abundant arterial blood. The blood supply of brain is supported by two arteries mainly: the left and right carotid artery. Therefore, the blood from those two arteries are usually used as the source of tracer in the technique of ASL. By inverting the magnetization of arterial blood in the region of carotid artery, after some time, the “labelled” arterial blood then flow into the brain and reach to the region that need to be imaged. The image that is acquired at this stage called the tag image because it contains the information of arterial blood that was labelled in the region of carotid artery.

On the other hand, in the second stage of acquisition, the acquisition method is similar to the first stage, but without the action of “labelling”. In other words, before acquiring the image in the imaging region, the magnetization of arterial blood was not inverted by RF pulse until it reaches the region of brain. In this stage of imaging, the image that is acquired called the control image. An example of the working principles of ASL is illustrated in figure 2.6.

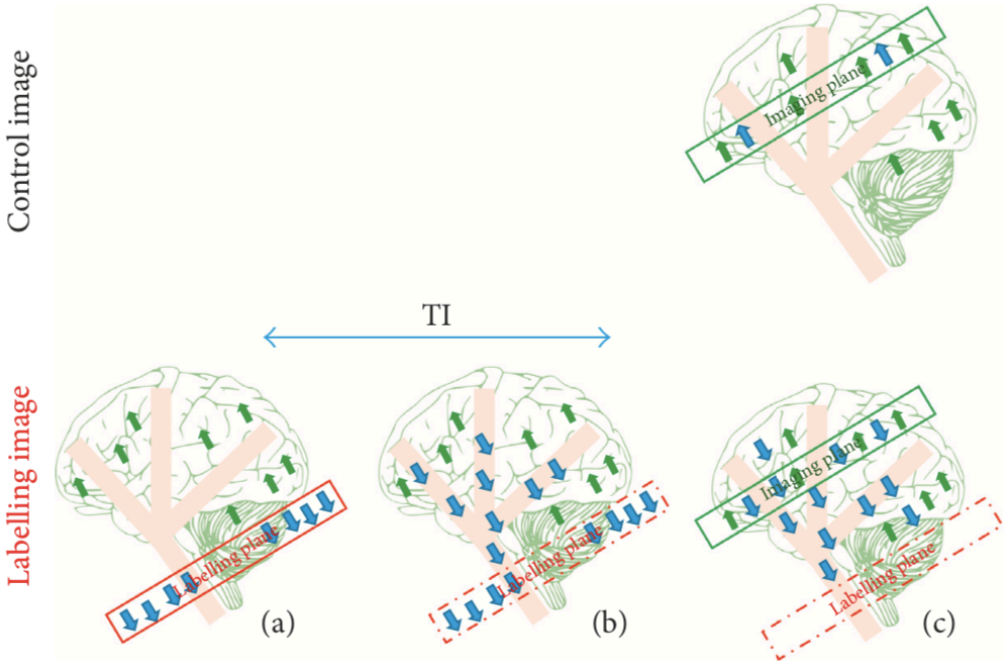

Figure 2.6: The working principle of ASL. In the labelling stage (lower row), the magnetisations of arterial blood are inverted within the labelling plane (red rectangular) (a), then the labelled arterial blood (blue arrows) flow into the brain tissue through the cerebral vasculature (b), the labelled arterial blood eventually reach to the imaging region after the certain TI (c). In the control imaging stage (upper row), until the magnetisation of all the arterial blood fully recover, the same imaging plane (green rectangular) is acquired again for the static brain tissue (green arrows) and the unlabelled arterial blood (blue arrow but parallel to the green one), Adapted from Alsaedi et al., 2018.

2.2.2 Tag-control image subtraction

After obtaining the tag and control image, since the magnetization of arterial blood had not been inverted before the acquisition of control image, the control image does not present the footprint of the labelled arterial blood. Therefore, a difference between the tag and control image should exist in terms of their signal intensity, although it is difficult to be observed by eyes. It is possible to make a subtraction of those image to see the difference, by subtracting the tag image form the control image, a difference of signal intensity can then be noticed (figure 2.7).

The signal difference image that is obtained from the subtraction, presents where the arterial blood delivered and accumulated in brain. Also, this signal difference image is proportional to the CBF, since the signal difference indicates the quantity of arterial blood that accumulates in the voxel. However, the signal difference is typically around 1-2%, since the amount of labelled blood that is delivered by perfusion is small compared with the total volume of blood in the brain tissue, causes the poor signal-noise-ratio (SNR) of the image and this is the main disadvantage of the technique of ASL.

Figure 2.7: Detectable ASL signal comes from the subtraction of control and labelling image. The resultant signal differences are proportional to the values of CBF. Adapted from Alsaedi et al., 2018.

2.2.3 Critical parameter in ASL acquisition

In the technique of ASL, there are some extra acquisition parameters that need to be considered carefully. During the first stage of acquisition, the labelling duration or known as bolus duration of arterial blood should be as long as possible in order to avoid the magnetization of blood recover fully when they reach to the region of brain.

On other hand, the post labelling delay (PLD) is also needed to be considered properly. PLD specifies the time duration that the arterial blood reach to the brain region, thus, the PLD should be long enough to let the arterial blood enter the imaging region, especially in pulsed-ASL (pASL), which is one of the ASL techniques and it will be described later, can apply multiple PLDs to investigate to behaviour of perfusion in different time point. The parameters above vary with the field strength, ASL method, and the blood flow velocity.

2.2.4 Different type of ASL

The technique of ASL can be classified in different methods: Continuous ASL (CASL), Pseudo-continuous ASL (PCASL), and Pulsed ASL (PASL), according to different manners of labelling and acquisition. An example of three different manners is illustrated in figure 2.8.

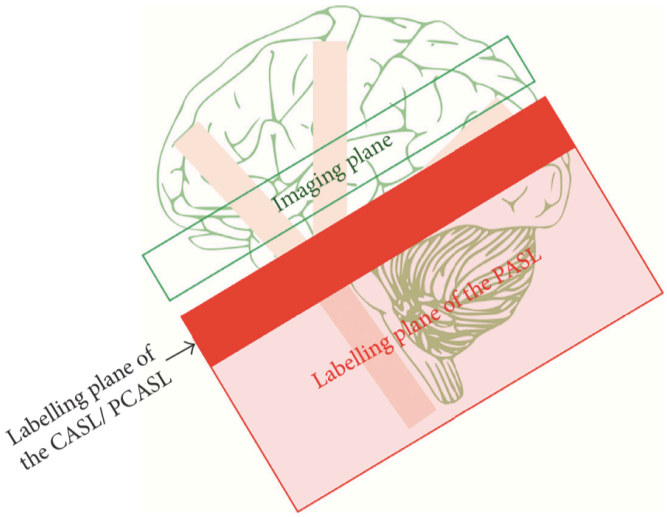

Figure 2.8: An illustration of the labelling manner is different ASL technique. In the manner of PASL, RF pulse is applied in a thick labelling plane and the labelling is nearly instantaneous. On the other hand, in the manner of CASL and PCASL, a thin labelling plane is used to apply RF pulse to label the arterial blood. As for the label duration, unlike the PASL, CASL and PCASL are applied a continuous RF pulse. However, in the case of PCASL, the long RF pulse is broken up in a series of repeating short RF pulses. Adapted from Alsaedi et al., 2018.

The CASL was introduced by Williams et al. in 1992, the oldest ASL technique. It applies a continuous RF pulse for a certain time period and a constant gradient to label the arterial blood in a relative narrow labelling plane. This manner can achieve a very efficient labelling, well-defined label duration and the long label durations. However, the main disadvantages of the manner are that the continuous RF pulse is difficult to be applied to the commercial clinical scanners and it is also difficult to achieve for multiple slice experiments because of the magnetization transfer effects, in which the signal of water is slightly reduced due to the interaction with other large molecules that are influenced by the labelling pulse (Chappell et al., 2018).

The manner of PCASL is similar to CASL that was mentioned above, it was introduced by Dai et al. in 2008, a modified version of CASL. Instead of using a long RF pulse like CASL, this manner separates the long RF pulse and gradient into a series of short repeating RF pulses and gradients. By having this feature, it is possible to reduce the error of phase tracking between RF pulse and flowing spins. Therefore, it is possible to be applied on the commercial clinical scanners, and results in well-defined label duration, relatively high labelling efficiency and well-matched control condition (Chappell et al., 2018; Alsaedi et al., 2018).

In CASL (the one was applied in this work), the RF pulse is applied to the magnetization of a slab of arterial blood for a relative short period of time instead of a narrow slice for a long period of time. The labelling of arterial blood is nearly instantaneous, about 10 ms in general. Furthermore, this technique can also be divided in three different acquisition methods: The Echo-Planar Imaging-based Signal Targeting Alternating Radiofrequency pulse (EPISTAR),

the Proximal Inversion with Control of Off-Resonance Effects (PICORE), and the Flow-sensitive Alternating Inversion Recovery (FAIR). In the manner of EPISTAR and PICORE, their labelling stage are same, but using different strategies for the control stage. In EPISTAR, the inversion pulse is applied above the imaging region; as for the PICORE, a non-selective inversion pulse is applied at the same frequency offset relative to the imaging region of the labelling stage, but without the spatial gradient. In the case of FAIR, the inversion is applied at the both side of the imaging region and using a non-selective on-resonance pulse for the control stage (Buxton, 2009).

The choice between the manner of EPISTAR, PICORE, and FAIR should depend on the direction of the arterial blood flow. If the direction of the arterial is unknown, FAIR maybe a better choice since it tags both side of the imaging region. If the direction of the arterial blood flow is known, PICORE could be an ideal choice since it tags the arterial blood from one side, especially for the brain perfusion imaging, in which the blood supply comes from the neck region only. Moreover, the PICORE has the advantage over the rest of them that this technique can avoid the venous artefact because of the absence of the spatial gradient during the control, preventing to image the venous blood that comes the top of imaging region. Unlike the EPISTAR and FAIR, the venous artefact can arise due to the use of superior control pulse and non-selective tagging pulse, respectively (Buxton, 2009). Therefore, the manner of PICORE was applied in this work, it was introduced by Wong et al. in 1997 to minimize the systematic errors in the quantification of perfusion that are caused by the spatially varying transit delay and the flow-through effect.

However, the labelling duration in this manner is unknown since it depends on the velocity of arterial blood, and their velocities are different in different individuals (Chappell et al., 2018). To solve this problem, the acquisition sequence QUIPSS II and Q2TIPS were developed to saturate the bolus at a specified time after labelling (Luh et al., 1999; Wong et al., 1997). These techniques cancel all the magnetization in the region of labelling, and thus the arterial blood that flow into the imaging region does not contribute to the ASL signal, therefore, the labelling duration can then be determined. In fact, the Q2TIPS is the improved version of QUIPSS II, by replacing the saturation pulse that is between the inversion RF pulse and the image readout sequence in QUIPPS II, with a series of narrow slice periodic saturation pulses train.

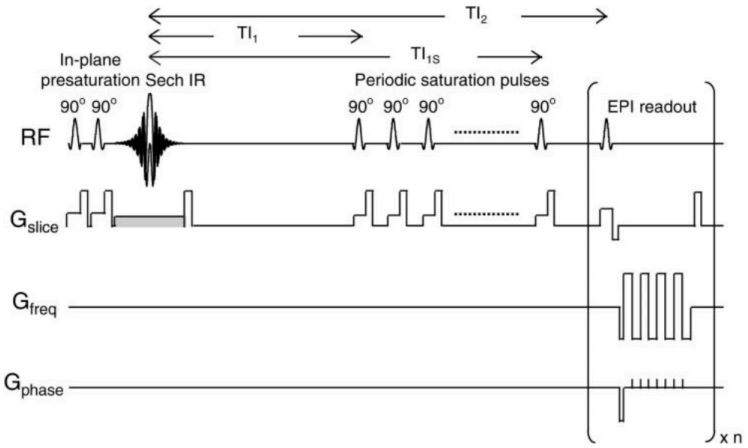

Figure 2.9: The pulse sequence of Q2TIPS is illustrated in this figure. At the beginning, double in-plane pre-saturation followed by a Sech inversion tagging pulse. The grey gradient is applied alternatively for switching the tagging and control imaging stage. Periodic saturation pulses are applied from TI_1 to TI_{1s}, consisting a series of 90° excitation pulses and each of them followed by a crusher gradient. A single or multi-slices EPI readout is then applied at TI_2, captured from Luh et al., 1999.

2.2.5 Kinetic model

As mentioned before, the signal difference that is resulted from the subtraction of tag and control image is proportional to the amount of arterial blood that accumulate in the voxel of brain image. In order to relate the signal difference and the CBF, it is necessary to describe the process of delivery and clearance of the arterial blood in time.

In this work, the *general kinetic model* for PASL that was introduced by Buxton et al. in 1998 was used. The PASL signal can be expressed by the general kinetic model (Buxton et al., 1998) and taking the form of (Chappell et al., 2010):

$$\Delta M_{tiss}(t) = \begin{cases} 0, & t < \Delta t \\ \dfrac{2\alpha M_{0a} CBF e^{-\frac{t}{T_{1app}}}}{R}\left(e^{Rt} - e^{R\Delta t}\right), & \Delta t \le t \le \Delta t + \tau \\ \dfrac{2\alpha M_{0a} CBF e^{-\frac{t}{T_{1app}}}}{R}\left(e^{R(\Delta t+\tau)} - e^{R\Delta t}\right), & \Delta t + \tau < t \end{cases} \tag{2.8}$$

with

$$R = \frac{1}{T_{1app}} - \frac{1}{T_{1a}} \tag{2.9}$$

and

$$T_{1app} = \frac{1}{T_1} + \frac{CBF}{\lambda} \tag{2.10}$$

Where Δt is ATT, M_{0a} is the equilibrium magnetization of arterial blood, τ is the bolus duration, and α is the inversion efficiency. By applying this kinetic model with the assumptions of the standard model, which was developed by several groups to emphasize the effect of transit delay from the tagging region to the imaged voxel (Buxton et al., 1998), the measured signal difference is therefore related to the CBF. However, the signal can be contaminated by the presence of labelled arterial blood in the large arterial vessel that is destined to the perfusion tissue in more distal region. Therefore, an extra macrovascular component of the general kinetic model was developed and it can be expressed by (Chappell et al., 2010):

$$\Delta M_{art}(t) = \begin{cases} 0, & t < \Delta t_a \\ 2\alpha M_{0a} e^{-\frac{t}{T_{1a}}} aBV, & \Delta t_a \leq t \leq \Delta t_a + \tau_a \\ 0, & \Delta t_a + \tau_a < t \end{cases} \tag{2.11}$$

Where Δt_a and τ_a represent the ATT and bolus duration of the labelled arterial blood, respectively. By applying this extra component to the general kinetic model, the arterial vessel wall is assumed to be impermeable and the arterial blood passes through the voxel instantaneously. The ATT in this component should be shorter than the one in the first component because of the velocity of arterial blood in large vessel is higher than the one in tissue capillary. Finally, the total signal from any voxel is the sum of the components above (Chappell et al., 2010).

2.2.6 Bayesian Inference

To estimate the perfusion parameters in this work, a probabilistic inference approach for non-linear models was used. This approach is based on Bayes' theorem, which determines the posterior probability distribution for the kinetic model by (Chappell et al., 2009):

$$P(w|y,M) = \frac{P(y,w|M)}{P(y|M)} = \frac{P(y|w,M)P(w|M)}{P(y|M)} \tag{2.12}$$

Where $P(w|y,M)$ is the posterior probability of the parameters given the data and the model, $P(y|w,M)$ is the likelihood of the data given the model, $P(w|M)$ is the prior probability of the parameter for the chosen model and finally the $P(y|M)$ is the evidence for the measurements given the model. This Bayesian approach incorporates with the characterization of signal and the gaussian distributed white noise (Chappell et al., 2009). Furthermore, the normalization of the posterior probability is ignored typically because of the calculation of variances and the

point estimation can be done without normalization. Therefore, the equation above can be simplified by taking out the term of evidence (Chappell et al., 2009):

$$P(w|y) \propto P(y|w)P(w) \tag{2.13}$$

This way, the posterior probability of the parameters given the data and the model is thus proportional to the likelihood of the data and the posterior probability of the parameters for the model (Chappell et al., 2009). The main advantage of this Bayesian approach is the incorporation of the prior information about the parameter based on physiologic knowledge, it is quite important for the ASL data that presents a poor SNR usually, therefore, the prior information can be used to regularize the problem by applying this approach.

3. METHODS

In this chapter, the methods of this work are presented, including the general information of the involved subjects, the method of image acquisition and the related parameters, the steps of data processing, estimation of brain perfusion and the further analysis. In principle, the experiment of this work was separated in few aspects mainly: data pre-processing, model fitting, measurement of region of interest (ROI), and statistical group analysis. The workflow of the work is presented schematically in figure 3.1.

On the other hand, all the subjects were scanned under both of the rest condition and the PDB condition. The subjects in the former condition were scanned without any instruction from the technician and breathed freely. The latter condition was executed with a set of breathing protocol to achieve hypocapnia. Also, the recording of $P_{ET}CO_2$ was performed in order to measure the concentration of CO_2 that was expired by subjects during the scanning of both conditions. More details about the preparation of experiment and the breathing tasks of subjects are presented in the following sections.

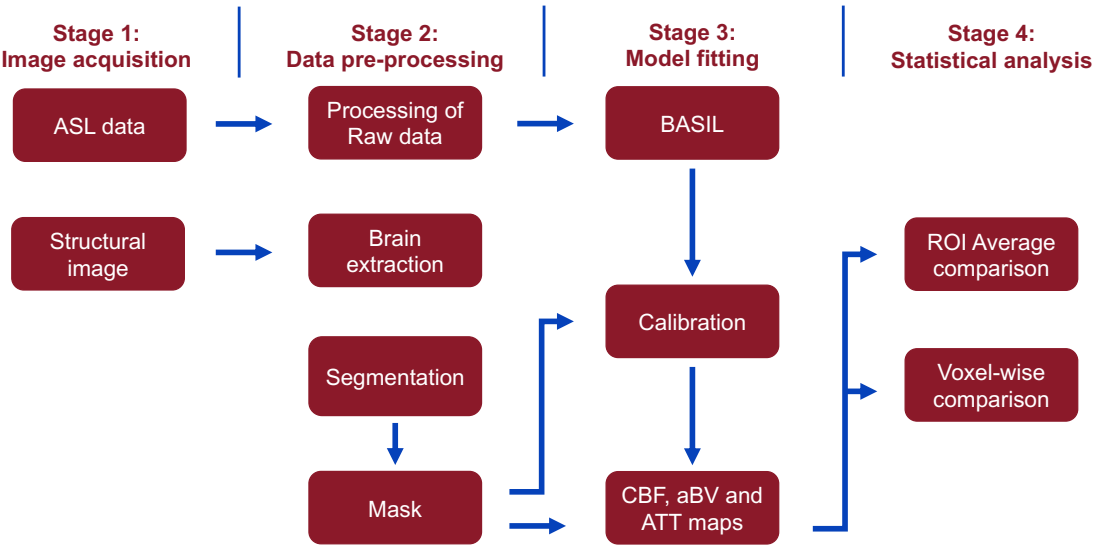

Figure 3.1: The brief workflow of this work. This work was separated in several stages: the image acquisition, data pre-processing, model fitting for the estimation of brain perfusion parameters, and statistical analysis.

3.1 Subjects and breathing task

A group of 13 healthy subjects was scanned at Hospital da Luz, All the subjects experienced 2 times of multi-PLD PASL acquisition, one for the REST condition and one for the PDB condition, respectively. As mentioned above, all the subjects were breathing freely during the

scanning of REST condition, they were also breathing rhythmically by following a breathing instruction during the scanning of PDB condition.

A set of breathing protocol was used for instructing the breathing of all the subjects during the period of PDB condition. A scheme of the breathing protocol is shown in figure 3.2. During the period of PDB condition, all the subjects needed to perform an inspiration for 2 seconds and an expiration for 3 seconds as a cycle, there were 8 cycles for each subject. The subjects were also asked to breathe more intensively than in REST condition. This breathing protocol was done by displaying visual instruction to the subjects during scanning using stimulus presentation software, NORDIC NEURO LAB's Nordic fMRI solution (www.nordicneru-olab.com).f

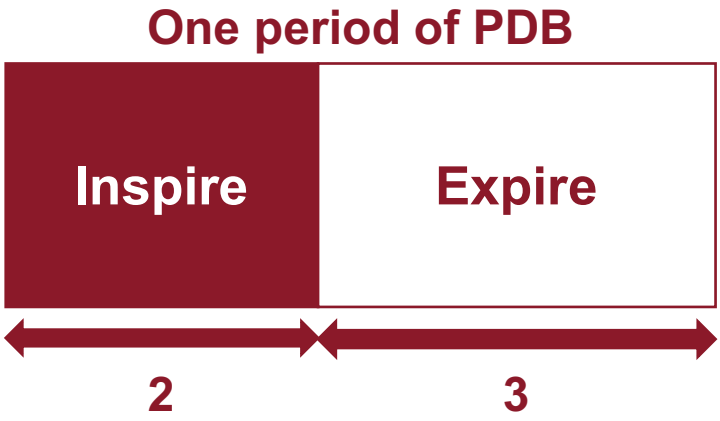

Figure 3.2: Illustration of the PDB breathing protocol used in this work. This breathing protocol took 2s for inspiring, 3s for expiring, and alternating with normal breathing. Each of the subject had to perform the protocol 8 times during the acquisition of PDB phase.

3.2 Image acquisition

A 3T MRI scanner (Verio, Siemens) and a 12 channel radiofrequency head coil were used for image acquisition of this work.

For the acquisition of PASL, as mentioned in the previous chapter, the PICORE-Q2TIPS sequence was used, with Gradient Echo EPI readout. The repetition time (TR) of 2500 ms and echo time (TE) of 19 ms (11 ms was used for 2 subjects) were used. On the other hand, the inversion times (TI_2) varied from 400 ms to 2400 ms in the steps of 200 ms were used, each control-tag pair repeated 8 times during the acquisition. A RF pulse of 10 cm thick labelling region was used, which was 18.8 cm below the first slice of the imaging region. The voxel size of 3.5 x 3.5 x 7 mm^3 was used for each subject. For 8 subjects, 9 continuous slices were acquired, obtaining a group of images with the image size of 64 x 64 x 9, for the rest of the

subjects, 28 continuous slices were acquired, yielding a group of images with the image size of 64 x 64 x 28.

T1-weighted structural image of each subjects was also acquired with MPRAGE sequence, with TR of 2250 ms, TE of 2.26 ms, 144 slices and voxel resolution of 1 x 1 x 1 mm^3. This high-resolution structural image can then be used for the purpose of image processing, more details are presented in the further section.

3.3 $P_{ET}CO_2$ recording

During the image acquisition, the end-tidal carbon dioxide pressure ($P_{ET}CO_2$) of each subject was monitored in both of the REST and PDB condition. 8 of the subjects were monitored using capnograph (Cap 10 Capnograph, Medlab GmbH), the rest of them were monitored using CO_2 monitor (PN 8050. Dräger, Lübeck, Germany). Both methods of monitoring were applied a nasal cannula to the capnograph and CO_2 monitor. The purpose of $P_{ET}CO_2$ recording was to obtain the level of pressure of CO_2 that expired by the subjects during scanning then correlating the value of $P_{ET}CO_2$ with the brain perfusion for the further analysis. The only thing should be noticed that when the PDB condition was acquired first, an additional break was necessary to place between the PDB condition and REST condition, guaranteeing the subjects of this imaging order could recover fully from the PDB condition so that the scanning of REST condition afterwards was no longer affected by hypocapnia.

After all the image acquisition and $P_{ET}CO_2$ recording, all the data were saved. The value of $P_{ET}CO_2$ recording of each subject in both conditions were then be processed. The mean value of each $P_{ET}CO_2$ recording and the Δ $P_{ET}CO_2$ of all the subjects between two conditions were also calculated. The Δ $P_{ET}CO_2$ was obtained by subtracting the $P_{ET}CO_2$ value of REST condition from the one of PDB condition. In principle, the Δ $P_{ET}CO_2$ should be a positive value due to the fact that the level of CO_2 is lower in hypocapnia compare with normocapnia.

3.4 Data pre-processing

In this section, the strategies and steps of data pre-processing are revealed. Including brain extraction, segmentation, registration between image spaces, calibration for equilibrium magnetization of the arterial blood, etc. In this step, the FMRIB Software Library, FSL (Jenkinson et al., 2012; Woolrich et al., 2009; Smith et al., 2004), was used to processing the ASL data. More details are presented in the following subsections.

3.4.1 Processing of images

Once the images were acquired, the first thing to do was to re-orientate the direction and size of all images. Among the raw image data, there must be some differences between all the subjects, for example, the size of head and the orientation of image, particularly in structural images, some of them even included the region of neck in their image. Therefore, it was necessary to re-arrange all the images in a same size and orientation.

On the other hand, for the ASL raw data, it was necessary to remove the first volume from the whole time series of image since the first volume of image was the calibration image during the scanning, thus, the raw data of each TI_2 were then modified to 16 volumes (8 pairs of tag-control image, 8 repeat times). After that, the modified raw data of each TI_2 were merged in one, obtaining a 4D ASL data with 176 volumes for the estimation of brain perfusion.

3.4.2 Brain extraction

Brain extraction is a common strategy in terms of the data processing in fMRI. Since the goal of this was to investigate the parameters of brain, such as brain perfusion, it was important to remove all the non-cerebral tissues and focus on the brain only, and these extracted brain images were useful in the further data processing steps. The FSL brain extraction tool (BET) (Smith, 2002) was used to perform brain extraction in this work, all the structural images were extracted with this tool, obtaining the whole clear brain and without any non-brain tissues, such as the skull. After extraction, all the resultant images were verified manually to see if the brains were extracted correctly. The examples of brain extraction are shown in figure 3.3.

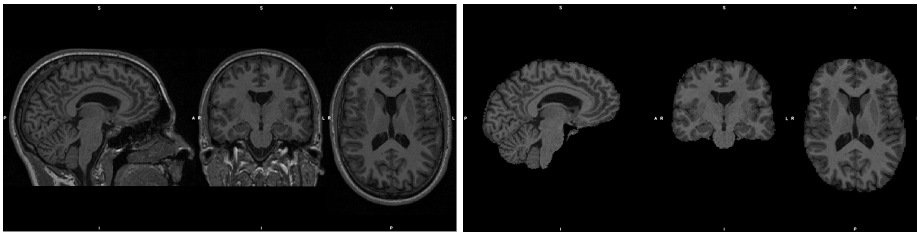

Figure 3.3: An example of brain extraction. The original T1 weighted brain image (left) and the extracted brain image (right), accomplished using the BET tool of FSL.

3.4.3 Segmentation

After the brain extraction, the extracted brains were used to perform the segmentation of grey matter (GM), white matter (WM), and cerebrospinal fluid (CSF) since those tissues are most relevant to the parameters of brain perfusion, but also useful for data analysis and calibration of image. The FMRIB's Automated Segmentation Tool (FAST) was applied for this processing stage, 3 partial volume images for the GM, WM, and CSF were obtained, respectively. However, among those partial volume image for each type of tissue, where each voxel contains a value in the range of 0-1 that represents the proportion of that tissue present in that voxel. Therefore, those partial volume images for different tissue needed to be extra processed in order to have an image with pure distribution of that tissue. More details of application and processing steps of the segmentation are explained in the further subsection.

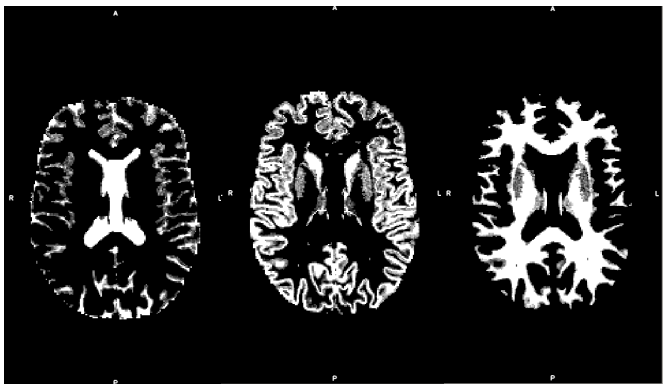

Figure 3.4: The segmented CSF (left), GM (middle), and WM (right) of a representative subject. Obtained using the FASL tool of FSL.

3.4.4 Registration

In the studies of fMRI, it is common to transform images between 3 spaces: the functional space, the structural space and the standard space. Transforming images between different spaces allows us to compare the image in one subject or across all the subjects, apply the information that extracted from structural image into functional image, and also useful for further analysis. For instance, the estimated perfusion maps need to be transformed into MNI 152 standard space for group analysis.

In this work, the FMRIB's Linear Image Registration Tool (FLIRT) was used to execute the registration. In principle, it determines the transformation matrix from one space to another space if the images of those 2 spaces are provided. The registration can also be executed inversely by inverting the transformation matrix. Furthermore, if an structural image of a subject is registered into both of the functional space and standard space, obtaining 2 transformation matrix, one for structural space to standard space, the other one for structural space to functional space, respectively, then the registration of that subject's images between

functional and standard space can be done by providing the obtained transformation matrix before, it is no necessary to perform registration from functional space to standard again.

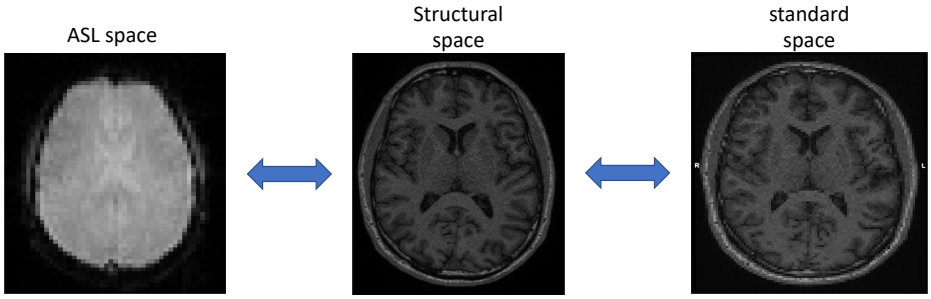

Figure 3.5: Illustration of registration between different image space.

At the very beginning of this registration step, all the structural high-resolution T1 weighted images were registered to the standard space based on the MNI 152 template, yielding the brain images in MNI template standard for all the subjects and the respective transformation matrix. The low-resolution 4D ASL data were also registered to the structural space based on the structural T1 weighted brain extracted images before running the model fitting. After that, the resultant estimated perfusion images were registered to the structural space and standard space, obtaining the estimated perfusion images in structural and standard space and the respective transformation matrix.

3.4.5 Calibration

In order to compare the estimated brain perfusion between the subjects, it was necessary to have a standard scale for all subjects to describe how does their perfusion behave, therefore, the calibration of equilibrium magnetization of the arterial blood (M_{0a}) was important in this work. Otherwise, the estimated brain perfusion presents the relative value of the perfusion intensity only, which is determined by the scanner type, instead of an absolute quantification. To achieve this purpose, there are several ways to calculate the M_{0a}.

In this work, several calibration methods were also tested to investigate their performance for calibrating CBF and aBV maps. Basically, there are two main manners to perform calibration for ASL data: the reference tissue-based and voxel-wise-based. The former estimates the M_{0a} by calculating the global mean M_0 of the reference tissue (figure 3.6), and the letter estimates the M_{0a} from the calibration image to image that needs to be calibrated voxel by voxel. In the case of reference tissue-based, the reference tissue can be CSF, GM, or WM, and the M_{0a} can then be calculated based on the M_0 of reference tissue:

$$M_{0a} = \frac{M_{0t}}{\lambda} e^{TE\left(\frac{1}{T_{2t}^*} - \frac{1}{T_{2a}^*}\right)} \tag{3.1}$$

Where the λ is the water partition coefficient of tissue-to-blood, the λ of CSF, GM, WM, and whole brain are 1.15, 0.98, 0.82, and 0.9, respectively (Herscovitch and Raichle, 1985), TE is the echo time of the sequence used, T_{2t}^* and T_{2a}^* are the T_2^* of reference tissue and arterial blood, respectively. The exponential term in this equation is a correction for T_2 or T_2 star decay.

Usually, the long TR image such as proton-density-weighted image is used as the calibration image for reference tissue-based method, since the proton-density-weighted image does not measure other physical properties such as T1, but the water content of subject, therefore, the proton-density-weighted image is frequently used because it reflects the concentration of water and thus the equilibrium magnetization. If the long TR image is not provided, the reference tissue-based method can also be executed by saturation recovery using the control image of the ASL raw data.

By using the saturation recovery, the signal from the calibration image can be expressed by the following equation:

$$M(t) = M_{0t}\left(1 - Ae^{\frac{-t}{T_{1t}}}\right) \tag{3.2}$$

Where the $M(t)$ represents the signal measured in the reference tissue, for example, CSF, and the M_{0t} represents the equilibrium magnetization of the reference tissue. The T_{1t} is the T_1 of the tissue and A is a constant describing the pre-saturation efficiency. This way, the M_{0t} can then be obtained by inverting the equation and substituting into the equation (3.1) to obtain the equilibrium magnetization of the arterial blood M_{0a}.

On the other hand, in the case of voxel-wise calibration, the calibration image can be the long TR image or the M0 image of the static tissue. Since the voxel-wise calibration calculates the M_{0a} and the resultant absolute CBF voxel by voxel, so that it is not necessary to specify a reference tissue or region for the reference M_0. The M_{0a} in this case can be calculated simply by:

$$M_{0a} = \frac{M_{0t}}{\lambda} \tag{3.3}$$

The equation (3.3) is similar to equation (3.1), the only difference is the exponential term for correction purpose. The M_{0a} in voxel-wise calibration does not have to be corrected since it is estimated in the same voxel as the perfusion, so the effect of T_2 or T_2 star on the static tissue is similar to the one on blood, thus it is usually ignored. However, before calculating the M_{0a}, the M_{0t} should be corrected if this static tissue image is acquired with a TR that is less than 5 second, and the correction is given by (Chappell, 2018):

$$\frac{1}{1 - e^{-\frac{TR}{T_1}}} \tag{3.4}$$

TR is the repetition time that is used for acquisition and T1 is that of the tissue. In the conventional readout, the static tissue in any voxel of the image can be related to the equilibrium magnetisation by (Chappell, 2018):

$$S = M_0 \left(1 - e^{-\frac{TR}{T_1}}\right) \tag{3.5}$$

This way, this manner solves and accounts for the partial saturation due to the relative short TR, the M_0 can then be estimated and therefore the M_{0a} according to equation (3.3).

Since the long TR calibration image was not provided, in this work, the calibration step was focused on saturation recovery only and compared in two different ways: reference tissue-based with control image from ASL raw data using the reference tissue of CSF, GM, WM; and voxel-wise-based using the reference of CSF and the image of M_{0t} that estimated from the equation 3.2. Within the manner of using saturation recovery to estimate the M_{0a}, it was divided in two ways: using the estimated saturation efficiency and fixing it to 100%, because the calibration used in this work estimates automatically the saturation efficiency by fitting the saturation recovery curve in BASIL, so it was necessary to compare the resultant M_{0a} from different saturation efficiency and the further impact on the absolute perfusion. Figure 3.7 illustrates schematically the procedure of calibration of this work.

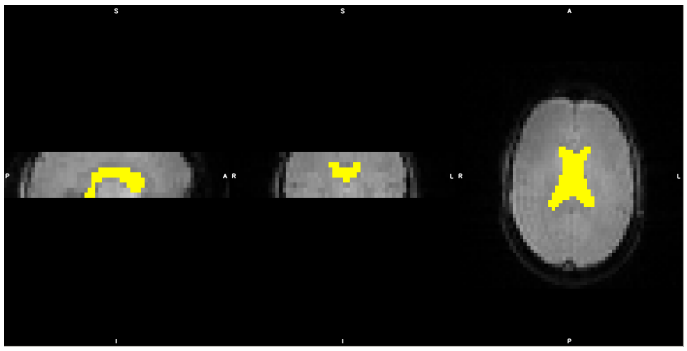

Figure 3.6: An example of specifying the reference tissue mask for calibration, CSF in this case (yellow parts).

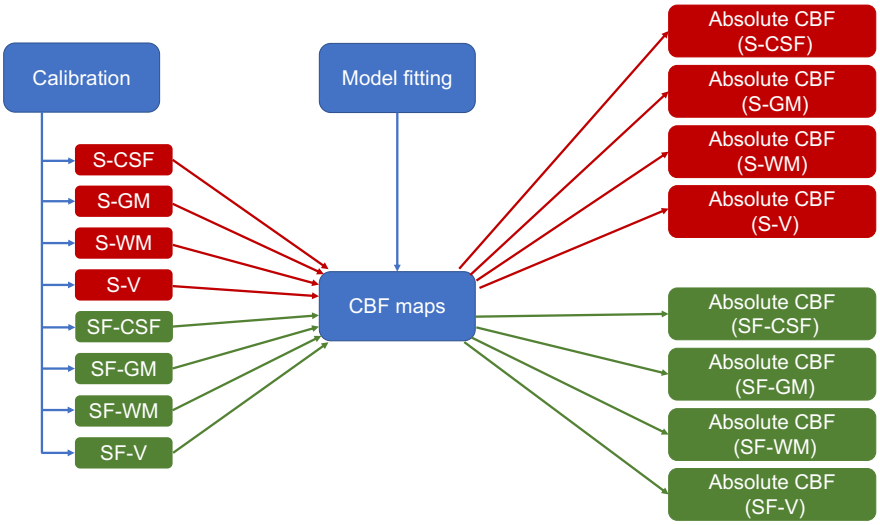

Figure 3.7: The workflow of calibration step in this work. 8 different way of calibration methods were applied to the CBF map that obtained from the model fitting, resulting 8 different CBF maps for each calibration method in each subject (S: Saturation recovery; SF: Saturation recovery with fixed saturation efficiency; V: Voxel-wise; CSF: Cerebral spinal fluid; GM: Grey matter; WM: White Matter).

8 combinations of calibration methods are shown in figure 3.7, they were saturation recovery using reference tissue CSF (S-CSF), GM (S-GM), WM(S-WM), voxel-wise (S-V), and saturation recovery with the fixed saturation efficiency using reference tissue CSF(SF-CSF), GM(SF-GM), WM(SF-WM), voxel-wise (SF-V), respectively. Each of the calibration methods calculated the absolute (calibrated) CBF map based on the original CBF map that came from model fitting, having 8 types of absolute perfusion maps finally.

This calibration step was done using the *asl_calib* of the BASIL toolbox. As mentioned in the previous section, all the tissue masks were segmented from the T1-weighted image of each subjects using FAST tool, after that, those tissue masks were then binarized with using *fsl_maths* tool, obtaining a binary tissue mask for each subject to perform the calibration. Applying the tissue mask into *asl_calib* and specifying the chosen tissue as the reference tissue for calibration, the M_{0a} of each subject was then be calculated and used for the further calculation of the absolute perfusion. Since this calibration step involved the control images of the ASL raw data, those control images needed to be extracted from the merged 4D ASL data of each subject that was mentioned before. The *asl_file* of BASIL toolbox was used to extract the control image from the merged 4D ASL data, obtaining an image with 88 volumes for the calibration step of each subject.

3.5 Region of interest and mask

As mentioned in the previous subsection, the grey matter (GM) was segmented from the structural image, resulting the image of GM. However, those were the partial volume images, which presented the percentage of the target tissue that located on a specific pixel (figure 3.4). In order to have a precise tissue mask, those GM masks of all subjects were from FAST segmentation needed to undergo an extra thresholding. By thresholding with the value of 1, it means that only the pixel with 100% of the target tissue can pass the filtration, having a pure tissue map without any contamination. These pure tissue maps were then be binarized, becoming the binary tissue masks for the ROI measurement.

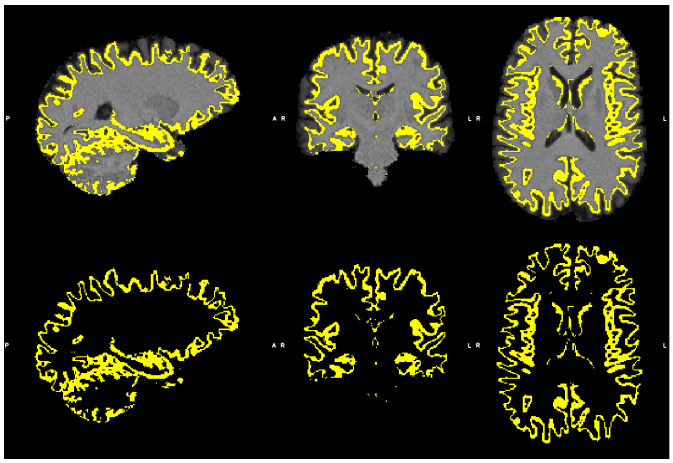

Figure 3.8: The applied GM mask of the representative subject. The GM mask was obtained from the segmentation step using FAST too of FSL.

For the measurement of the ROI, all the masks that mentioned above were applied on the estimated perfusion maps that were resulted from the model fitting, taking the mean values and standard deviations of the non-zero pixels. The results of measurement and comparison are shown in the next section. In this processing step, the *fsl_maths* tool was used for thresholding and binarizing of images.

3.6 Estimation of perfusion parameters

After the pre-processing steps, all the image data were ready for estimation of brain perfusion parameters. In this stage, several things needed to be determined properly to have a precise estimation of parameters, such as the priors and the options of analysis within the model fitting. More details are revealed in the following subsection.

3.6.1 Priors

Before estimating the value of perfusion parameters, the prior of parameters should be well defined, as the inputs for model fitting. The priors that were used in this work, were according to the prior values that presented by Chappell et al. in 2010 and they are shown in table 3.1.

Among the parameters, a noninformative prior was used for CBF to reflect that there were no prior assumptions for this value; for the temporal parameters, their priors were determined restrictively to reflect the physiological characteristic of the values. For example, the prior of T_1 and T_{1a} were determined based on their physiological feature, reflecting the high certainty of the values but keep expecting their local variation (Chappell et al., 2010).

Different form the priors of bolus duration that were used by Chappell et al., both of the arterial and tissue bolus duration were set to 0.75 second according to the previous study since the Q2TIPS was used for longer PLD in this work (Sousa et al, 2014a). Moreover, the selection of tissue and arterial BAT depends upon the manner of acquisition, such as the gap between tagging and imaging region (Chappell et al., 2010), and the arterial BAT was set to 70% of the tissue BAT due to the assumption of their relationships from the previous studies (Sousa et al, 2014a; Ho et al., 2011).

Table 3.1: Priors for model fitting in this work. The parameter of $f, \Delta t, aBV, \tau, T_1$ represent the perfusion, arterial transit time (ATT), arterial blood volume (aBV), bolus duration, and T1 of the brain tissue, respectively. The rest of the parameters are the physiological parameters of the arterial, such as the T1, ATT, and arterial bolus duration. on the other hand, the variance of automatic relevance determination (ARD) was applied to the parameter of aBV to control the component of the kinetic model and thus the model complexity.

Parameter	Mean	Standard deviation
f (ml/g/s)	0	10^3
Δt (s)	0.7	0.3
aBV (%)	0	ARD
τ (s)	0.75	0.3
T_1 (s)	1.3	0.1
T_{1a} (s)	1.6	0.1
Δt_a (s)	0.5	0.3
τ_a (s)	0.75	0.3

For the parameter of aBV, an automatic relevance determination (ARD) was applied, since the fitting of intravascular component with 3 additional parameters in the tissue only voxel could result in overfitting, leading to arise the artefactual intravascular signal. The ARD automatically controls the number of components in the current model and therefore the model

complexity. In this manner, the mean value of aBV was set to 0 and its variance was set as a further parameter to be determined from the data. For instance, in the situation of obtaining a large variance from estimation, the prior of aBV can then be assumed as noninformative prior; in the case of the variance becomes smaller, then the prior becomes informative until adequately small and forces the aBV to 0 (Chappell et al., 2010).

3.6.2 Model fitting

After defining the priors for the parameters and inputting to the model, the estimation of brain perfusion parameters was then be accomplished. In this step, the model fitting was performed using oxford_asl of the BASIL toolbox (Chappell et al., 2009), by adjusting the priors and options such as spatial regularisation (Grove et al., 2009) through the command line. It can also be done by using the graphic user interface of the same programme asl_gui, however, oxford_asl is flexible than the other one in terms of the advanced options for estimation and the users can adjust manually, which cannot be done in the graphic user interface. Furthermore, the calibration of the perfusion parameters can be performed simultaneously within oxford_asl.

Besides the priors, few analytical options needed to be considered before executing the model fitting. These options can offer some additional corrections or incorporation with some special parameters and condition during the estimation, such as the correction for arterial or macrovascular contamination, motion correction, partial volume correction, incorporate with T1 uncertainty, and fix the label duration.

For the output of model fitting, it provides 3 types of images mainly, the perfusion map of CBF, ATT, aBV, and they were accompanied by their variance and normalised maps, respectively. If the registration and calibration were performed within the model fitting, the calibrated version of those parameters' map could be obtained and transformed in structural and standard space.

3.7 Data analysis

By executing the model fitting, the perfusion map of CBF, ATT, and aBV were obtained. The next step was to verify all the results to see if they were processed correctly, and compare the perfusion parameters between the condition of baseline and hypocapnia. In this stage, few aspects of analysis were performed, the ROI comparison, $P_{ET}CO_2$ comparison, and voxel-wise analysis using nonparametric permutation inference approach and general linear model (GLM).

For the ROI comparison, all the original perfusion maps that were from model fitting, were transformed to structural space and measured within the GM that mentioned previously. By obtaining their mean values within the tissue masks, the CBF, ATT, and aBV were then be compared within a subject or cross the subjects. A paired T-test was performed for the statistical analysis of the ROI comparison to see if there was a significant difference within the selected ROI in terms of the perfusion parameters.

In the analysis of functional MRI, it is usually divided into model-based and model-free methods. The GLM is a model-based method, and also the most common manner for function MRI data analysis, which sets up a model with a general pattern that is expected to see in the data and fits it into the data. For example, if a model is designed from timing of a stimulation that was used during MRI scanning, then a good fit between the designed model and the current data represents the data that resulted from scanning was likely caused by the stimulation, and thus a significant result (Smith, 2004).

On the other hand, the voxel-wise analysis was performed using the *FSL randomise tool* (Winkler et al., 2014) by incorporating GLM to carry out the statistical analysis. In general speaking, this nonparametric permutation inference approach can provide a statistical analysis, which compares the images voxel to voxel to locate the difference within the subject or cross the subject. In this approach, 3 different manners are available to perform the analysis: simple voxel-wise, cluster-based thresholding, and threshold-free cluster enhancement. The last manner was considered in this work.

Threshold-Free Cluster Enhancement (TFCE) (Smith and Nichols, 2009) is a new method that based on the normal cluster-based thresholding technique, having the sensitivity advantage of cluster-based thresholding, while avoiding the limitation of defining the initial cluster forming threshold, the instability in overall processing chain that is introduced by initial hard thresholding, and the arbitrary spatial smoothing.

4. RESULTS

In this chapter, the results of this work are presented, using the methods described in the previous chapter. This chapter will be focused on 3 main aspects, the result of $P_{ET}CO_2$ recording of each subject during the MRI acquisition, the results of BASIL and the ROI comparison, and the comparison of calibration methods are presented.

4.1 $P_{ET}CO_2$ recording

Table 4.1: The mean value and difference of $P_{ET}CO_2$ of each subject during the acquisition of different condition. * denotes the significant differences ($p < 0.05$).

Subjects	$P_{ET}CO_2$ mean PDB	$P_{ET}CO_2$ mean REST	$P_{ET}CO_2$ Difference
S1			2.70
S2			8.00
S3			0.80
S4			3.70
S5			1.20
S6	6.08	14.05	7.98*
S7	31.81	31.41	-0.40
S8	19.20	16.32	-2.88
S9	20.64	22.28	1.64*
S10	16.95	21.53	4.58*
S11	11.73	13.59	1.86*
S12	13.12	12.98	-0.14
S13	15.47	18.20	2.73*

Among the table above, the mean value of $P_{ET}CO_2$ of each subject during PDB and REST are shown, also the difference of those mean $P_{ET}CO_2$. Showing that subject 6, 9, 10, 11, and 13 had a significant difference of $P_{ET}CO_2$ between 2 condition, that means these subjects achieved hypocapnia during the experiment. However, some of the subjects did not show a significant difference, even the negative values. Indicating that those subjects did not achieve hypocapnia, since the build-up process for hypocapnia in every person could be different. Also, the $P_{ET}CO_2$ value of subject 1 to 5 was not provided, therefore, according to the incomplete information of $P_{ET}CO_2$, this information could be a reference value for the further results only.

Despite the negative difference in some subjects and the lack of information, the data of those subjects were useful and still be processed, since the objective of this work was not only focus

on whether the hypocapnia was achieved successfully, but also to quantify the perfusion parameters and compare the different calibration methods.

4.2 Perfusion parameters measurement and group analysis

In this section, the results from model fitting are presented, including the CBF map, ATT map, and aBV map of each subject. Figure 4.1 presents those parameters map of subject 13 that resulted from the BASIL in structural space. More resulted images are presented in appendix for simplicity reason.

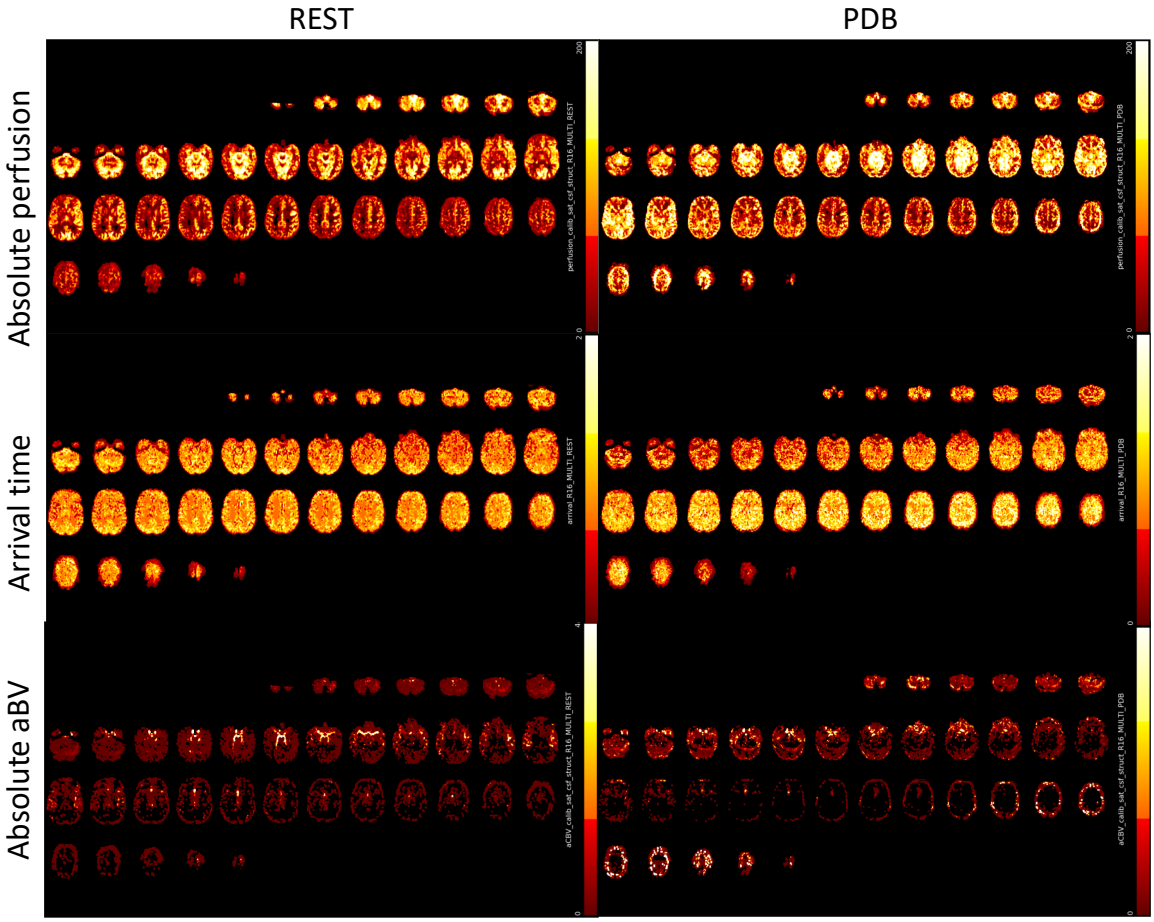

Figure 4.1: CBF (upper row), ATT (middle row), aBV (lower row) map of S1 in during REST (left column) and PDB (right column).

4.2.1 ROI comparison

Table 4.2 The mean value of the perfusion parameters' map of each subject within the GM mask during the breathing task of REST and PDB. The absolute values of CBF and aBV in this table were obtained using saturation recovery with the reference tissue of CSF.

Subjects	CBF (ml/100g/min)		ATT (s)		aBV (%)	
	REST	PDB	REST	PDB	REST	PDB
S1	69.50	77.42	0.75	0.77	0.32	0.45
S2	74.72	73.93	0.76	0.74	0.41	0.35
S3	83.95	59.59	0.75	0.72	0.49	0.67
S4	72.17	75.29	0.73	0.71	0.39	0.34
S5	66.01	69.52	0.59	0.62	0.51	0.63
S6	78.87	97.30	0.64	0.81	0.92	0.66
S7	95.87	90.52	0.78	0.74	0.68	0.66
S8	102.95	134.36	0.77	0.81	0.55	0.61
S9	58.50	48.87	0.85	0.80	0.12	0.14
S10	30.15	40.69	0.75	0.77	0.07	0.13
S11	44.43	37.60	0.80	0.74	0.13	0.09
S12	62.05	65.39	0.89	0.82	0.14	0.14
S13	81.82	105.45	0.92	0.96	0.19	0.90
Mean ± SD	70.8±18	75.1±26	0.7±0.2	0.8±0.1	0.4±0.2	0.4±0.3

The ROI comparison between REST and PDB group was achieved by obtaining the three parameter maps of CBF, BAT, and aBV, then measured the value within the GM mask. The results of measurement are shown in table 4.2. Among the table above, the mean values of REST and PDB condition of each subject are shown. In principle, the values in PDB should be lower than the one in REST for the CBF and aBV map, however, within most of the subjects, the mean values of CBF and aBV map in PDB were higher than in REST. On the other hand, the mean values of ATT were also obtained, showing that the group mean of PDB was higher than the group of REST. A paired t-test was performed for the group mean values obtained above and indicating that there was no significant different between REST and PDB group (CBF: $p = 0.32$; aBV: $p = 0.30$; ATT: $p = 0.89$). The bar chart of the mean value of CBF, ATT, and aBV for all subjects are displayed in figure 4.2.

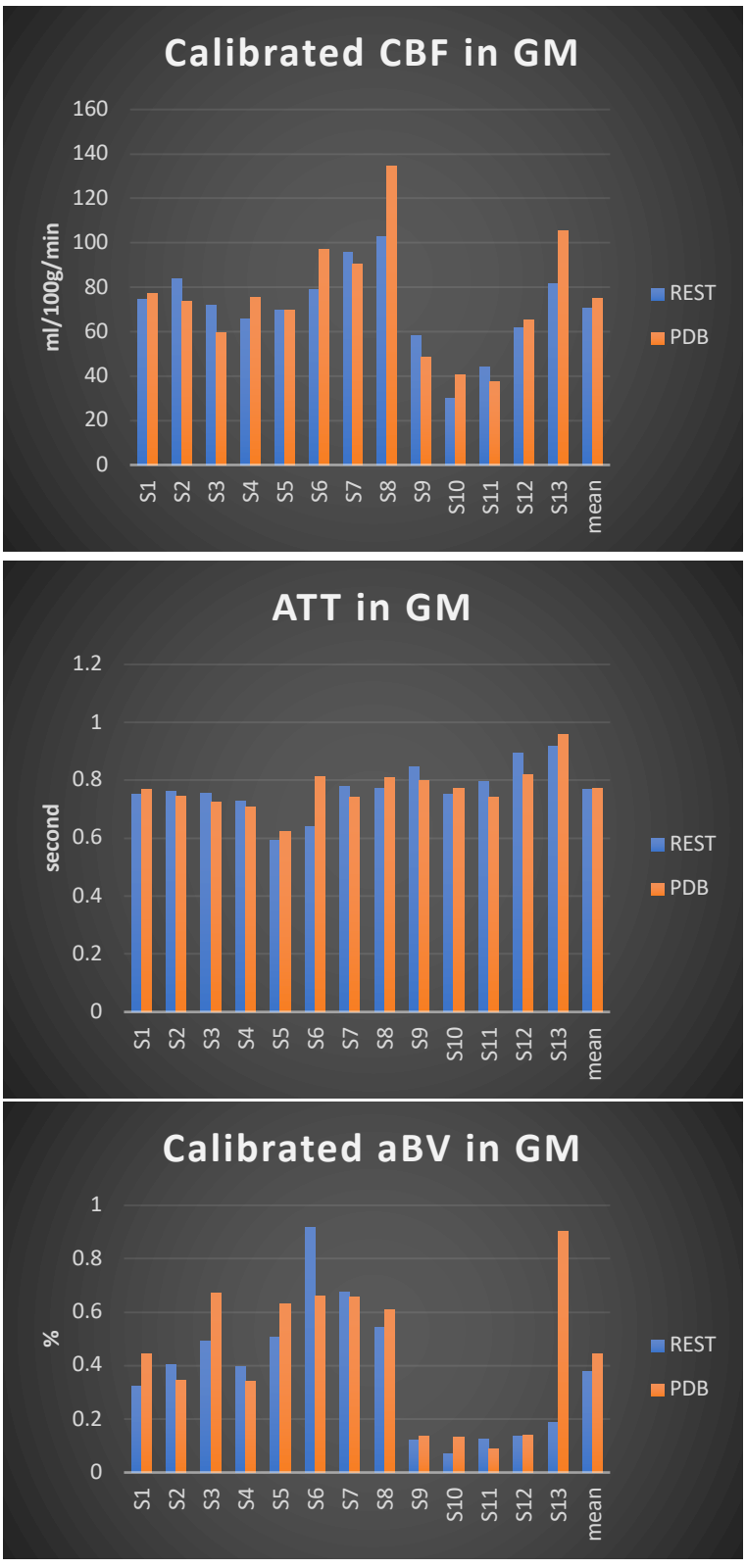

Figure 4.2: The bar chart of the mean value of CBF (top), ATT (middle), and aBV (bottom), obtained within GM mask.

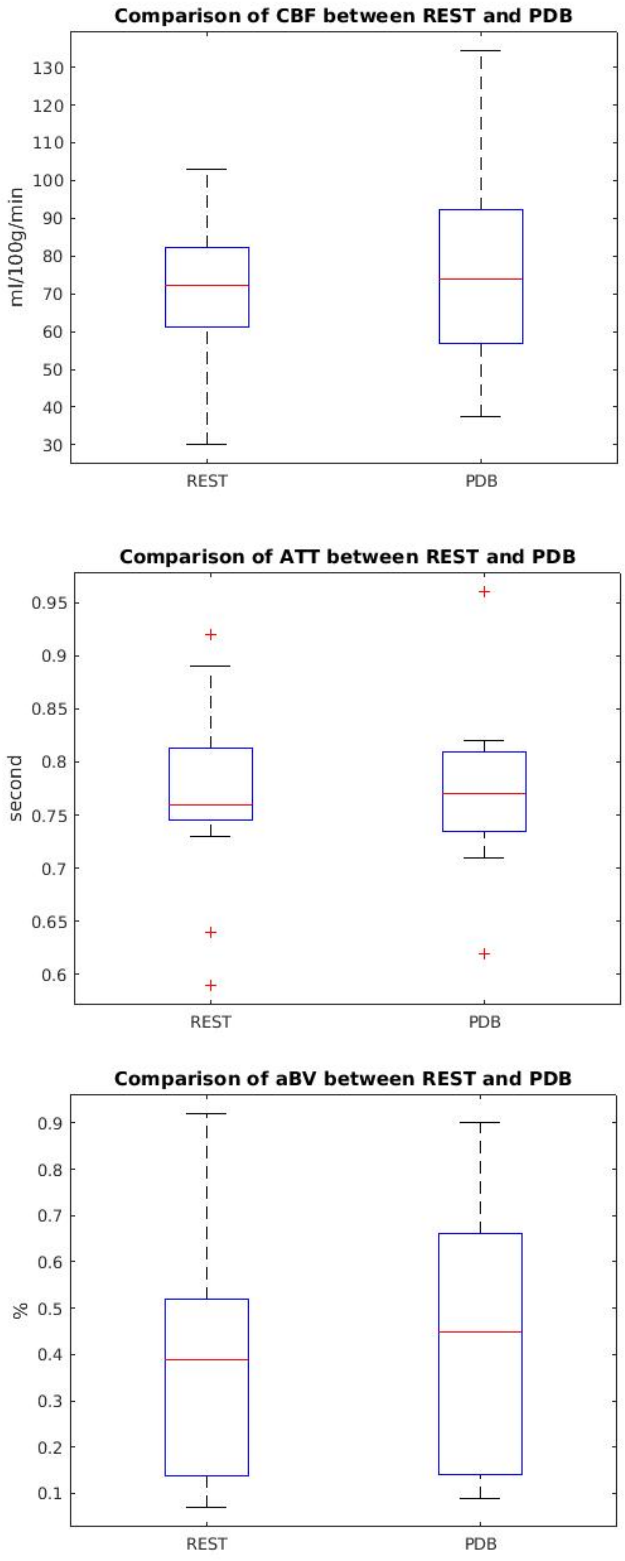

Figure 4.3: The boxplot of the mean value of CBF (top), ATT (middle), and aBV (bottom), obtained within GM mask.

The observation of group mean values might not reflect comprehensively the difference between 2 condition within subject. 3 boxplots are shown to compare the distribution of the value in each voxel between conditions in each subject, within GM mask. Figure 4.3, 4.4, and 4.5, present the comparison of CBF, ATT, and aBV map, respectively, in both conditions for each subject in a boxplot, the values were obtained within the GM mask.

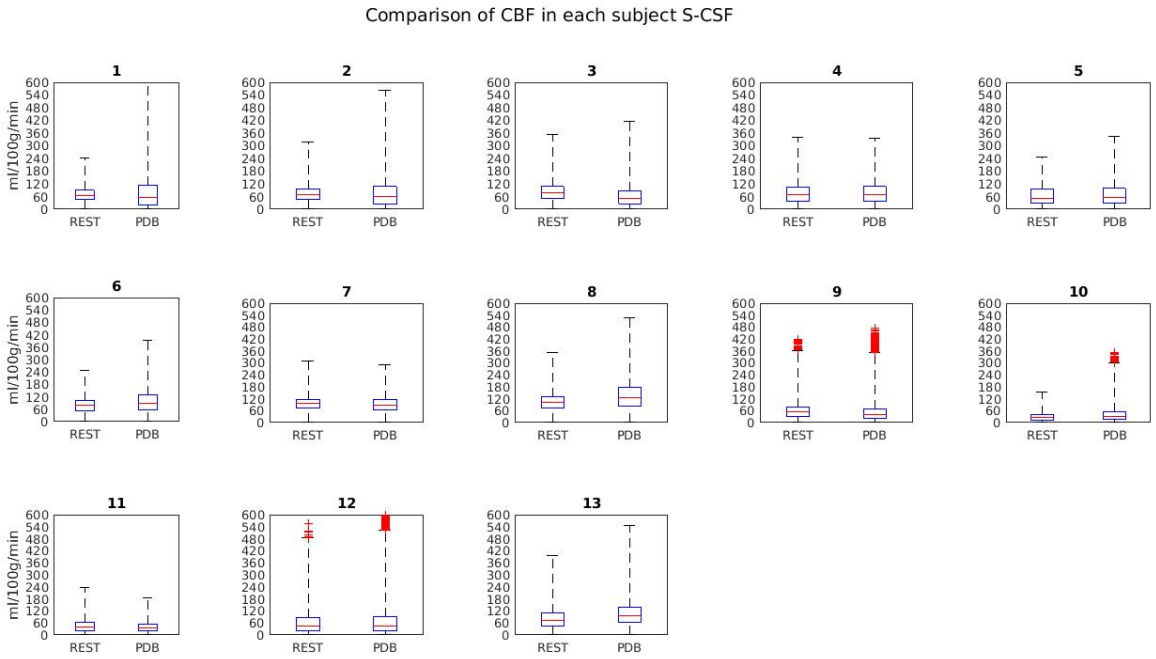

Figure 4.4: A boxplot of CBF map of each subject in REST and PDB condition, obtained within GM mask.

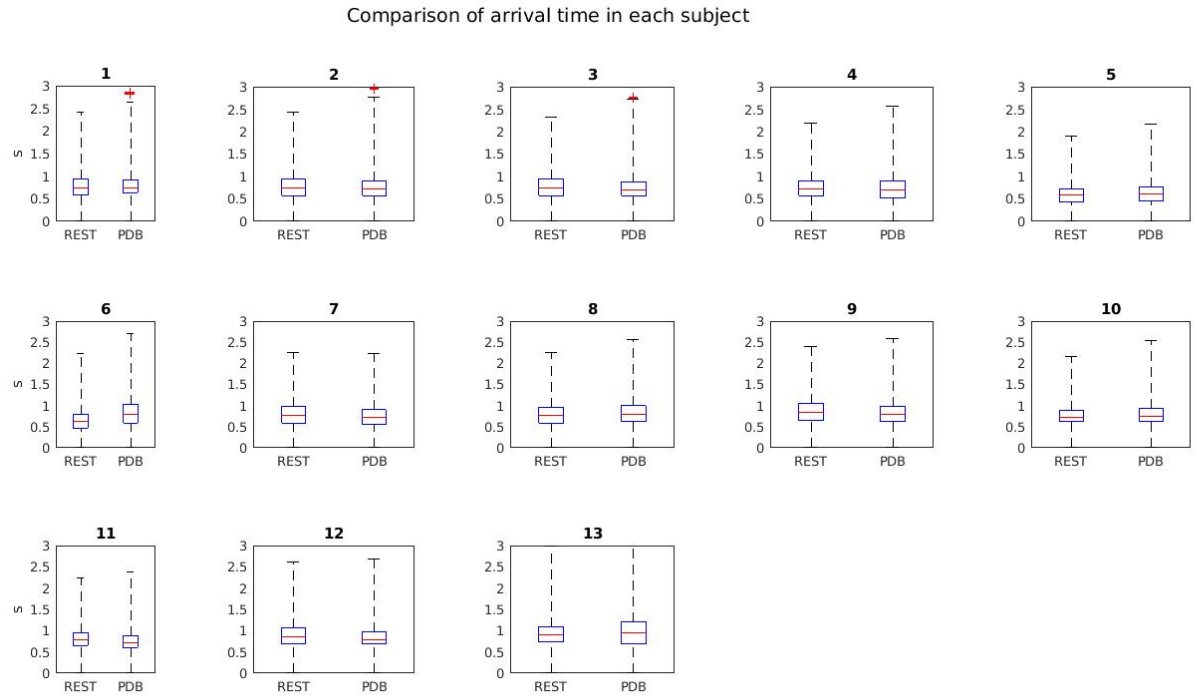

Figure 4.5: A boxplot of ATT map of each subject in REST and PDB condition, obtained within GM mask.

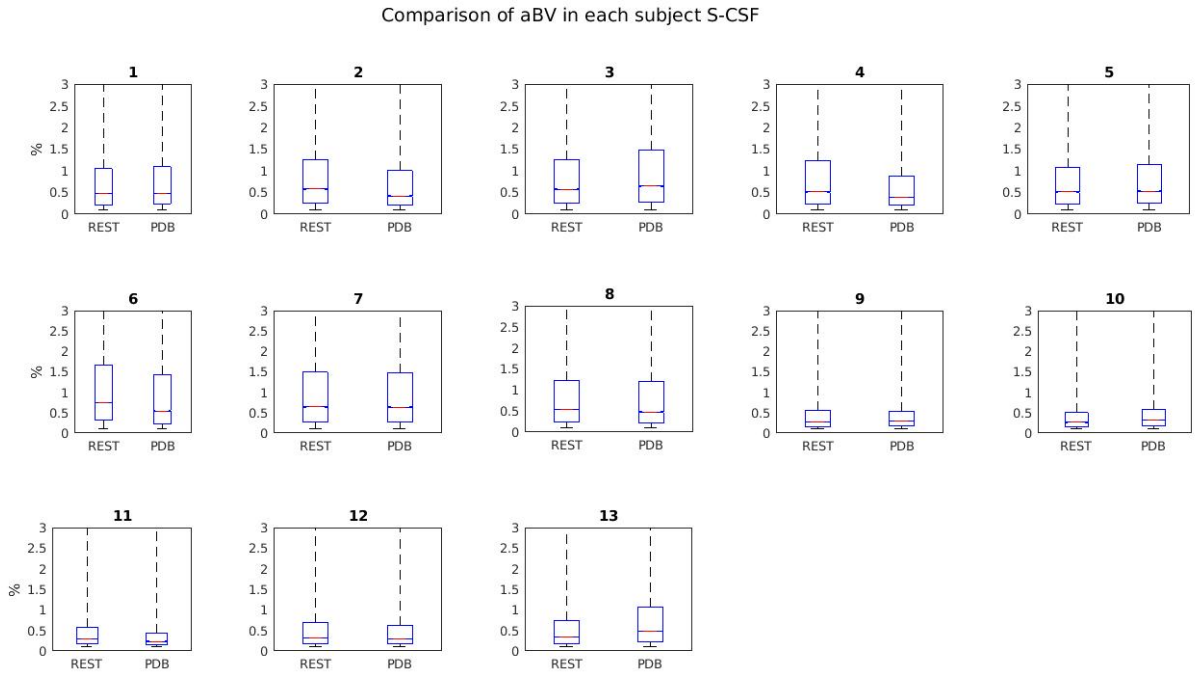

Figure 4.6: A boxplot of aBV map of each subject in REST and PDB condition, obtained within GM mask.

4.2.2 Voxel-wise comparison

In order to see if there were significant differences between two conditions, a whole brain voxel-wise comparison was necessary to perform. The statistical results that supposed to discuss in this subsection was achieved using FSL randomise tool with the technique of Threshold-Free Cluster Enhancement (TFCE). However, the corrected and uncorrected results from TFCE indicated that there was no significant difference in CBF, ATT, and aBV between REST and PDB group, therefore, no images or figures were shown in this subsection because they were basically empty.

4.3 Comparison of calibration methods

In this section, the comparison of different calibration methods is presented. They were saturation recovery using reference tissue CSF (S-CSF), saturation recovery using reference tissue GM (S-GM), saturation recovery using reference tissue WM (S-WM), saturation recovery using voxel-wise method (S-V), saturation recovery with fixed saturation efficiency using reference tissue CSF (SF-CSF), saturation recovery with fixed saturation efficiency using reference tissue GM (SF-GM), saturation recovery with fixed saturation efficiency using reference tissue WM (SF-WM), and saturation recovery with fixed saturation efficiency using voxel-wise method (SF-V). These calibration methods were used to calculate the absolute CBF for each subject in REST group.

Table 4.3: The equilibrium magnetisation of arterial blood estimated from different calibration methods and multiple reference tissues. (S: Saturation recovery; SF: Saturation recovery with fixed saturation efficiency; V: Voxel-wise; CSF: Cerebral spinal fluid; GM: Grey matter; WM: White Matter)

Subject	M0a							
	S-CSF	S-GM	S-WM	S-V	SF-CSF	SF-GM	SF-WM	SF-V
1	447.44	589.45	807.65	584.53	1263.32	579.52	787.12	575.35
2	511.16	686.44	934.00	676.87	1440.01	672.48	909.65	664.09
3	554.24	742.49	987.68	727.05	1569.68	729.00	963.70	715.13
4	527.51	610.13	892.72	655.22	1515.09	603.69	873.41	648.32
5	603.17	721.11	1003.52	748.10	1727.35	710.32	980.25	737.49
6	591.64	878.03	1124.47	835.06	1666.84	859.98	1096.59	819.75
7	599.64	854.38	1120.95	846.07	1717.29	838.76	1094.87	831.84
8	627.39	882.77	1150.15	861.42	1789.33	864.66	1123.09	846.12
9	642.43	824.33	1043.98	748.13	1888.50	817.93	1029.33	744.71
10	631.44	827.89	1095.17	768.7	1849.96	821.10	1079.91	764.42
11	626.13	922.20	1192.66	815.01	1836.14	912.11	1175.53	809.08
12	823.61	1042.40	1336.18	918.33	2460.03	1029.66	1314.41	909.01
13	810.36	1033.52	1300.24	901.67	2369.57	1020.26	1278.83	892.01
Mean ± SD	615.09±105	816.55±142	1076.11±153	775.86±99	1776.39±334	804.57±141	1054.36±153	765.95±98

Table 4.3 presents the equilibrium magnetisation of arterial blood estimated from different calibration methods. The highest and lowest for each subject were observed in SF-CSF and S-CSF, respectively. The M0a were then used to calculate the absolute CBF for each subject and compared their values. Table 4.4 shows the mean value of the absolute CBF maps that calculated by the M0a from table 4.3.

Among table 4.4, the highest and lowest value of calibrated CBF in each subject were found in the manner of S-CSF and SF-CSF, respectively. This result was reasonable because the absolute CBF were calculated through dividing the relative CBF map by M0a and times 6000, therefore, the higher / lower the M0a, the lower / higher the resultant absolute CBF value.

Table 4.4: The absolute CBF calculated using the equilibrium magnetisation of arterial blood from table 4.3, using different calibration methods and multiple reference tissues. (S: Saturation recovery; SF: Saturation recovery with fixed saturation efficiency; V: Voxel-wise; CSF: Cerebral spinal fluid; GM: Grey matter; WM: White Matter)

Sub-ject	**Absolute CBF (ml/100g/min)**							
	S-CSF	S-GM	S-WM	S-V	SF-CSF	SF-GM	SF-WM	SF-V
1	66.49	38.50	52.75	55.49	24.61	53.66	39.51	38.50
2	74.72	40.89	55.64	57.84	24.52	56.79	41.98	40.89
3	83.95	47.11	62.66	65.94	29.64	63.82	48.28	47.11
4	72.17	42.65	62.40	65.34	25.13	63.07	43.59	42.65
5	66.01	39.68	55.22	55.13	23.05	56.08	40.62	39.68
6	78.87	41.50	53.15	53.72	30.00	54.26	42.55	41.50
7	95.87	51.29	67.29	66.54	33.48	68.54	52.51	51.29
8	102.95	56.16	73.17	73.22	36.10	74.70	57.51	56.16
9	58.49	36.00	45.59	46.95	19.90	45.95	36.51	36.00
10	30.15	17.38	23.00	24.49	10.29	23.19	17.63	17.38
11	44.43	23.33	30.17	32.05	15.15	30.50	23.67	23.33
12	62.05	38.24	49.02	52.05	21.24	49.63	38.88	38.24
13	81.82	50.99	64.15	67.33	27.98	64.99	51.85	50.99
Mean ± SD	70.61±19	40.29±10	53.40±14	55.08±14	24.70±7	54.24±14	41.16±11	40.29±10

After calculating the absolute CBF, the one-way ANOVA statistical analysis was used to test the calibration methods through the resultant absolute CBF values. A boxplot was outputted from the statistical test and presented in figure 4.6. Showing a significant difference between 8 types of calibration methods with the p value equals to 1.36E-12. A multiple comparison was then performed, indicated that the method of S-CSF was significantly different from all the calibration methods except the method of S-V, and the method of SF-CSF was significantly different from all the calibration methods except the methods of S-GM and SF-V, however,

any significant different was not found between the methods of S-GM, S-WM, S-V, SF-GM, SF-WM and SF-V.

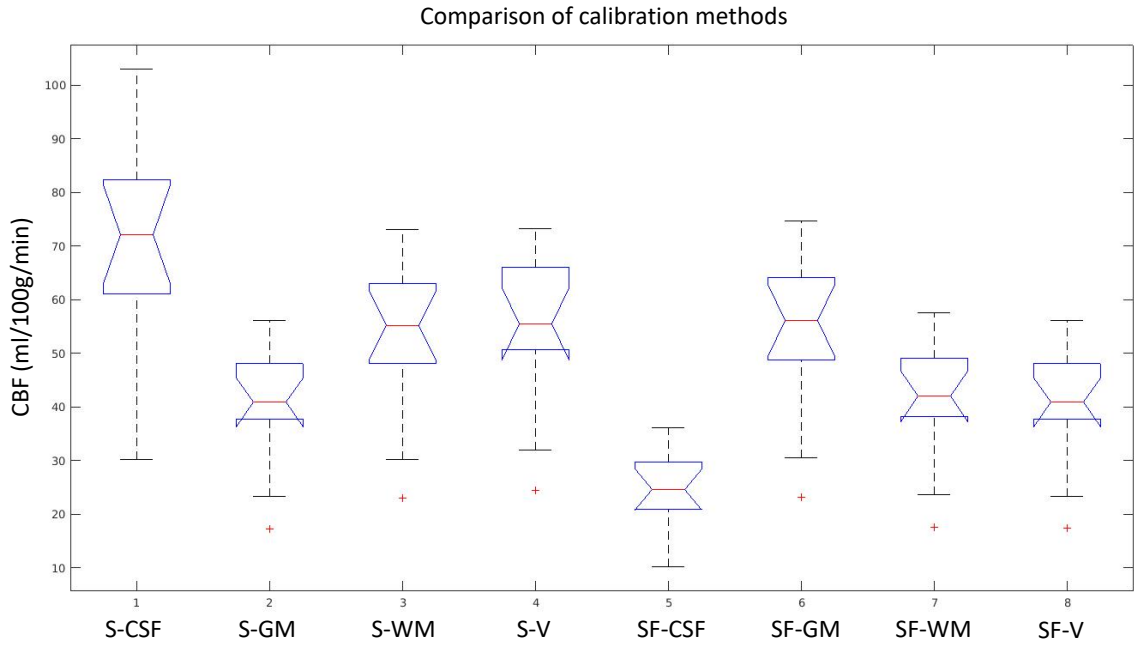

Figure 4.7: The boxplot of the absolute CBF values resulted from different calibration methods, obtained from one-way ANOVA statistical test, indicating that the value of CBF resulted from the method of S-CSF was significantly higher than the others, except the calibration using S-V; and the one resulted from the method of SF-CSF was significantly lower than the others, except the calibration using S-GM and SF-V. No significant differences were found between the calibration method of S-GM, S-WM, S-V, S-GM, SF-WM, SF-V. (S: Saturation recovery; SF: Saturation recovery with fixed saturation efficiency; V: Voxel-wise; CSF: Cerebral spinal fluid; GM: Grey matter; WM: White Matter)

5. CONCLUSIONS

In summary, this work investigated the behaviour of brain perfusion during the subject performed the paced deep breathing task and normal breathing, and the brain perfusion parameters were quantified successfully using multi-PLD arterial spin labelling MRI and BASIL with general kinetic model. Also, the current FSL tools were tested in order to find a best way to process the functional MR image.

Although the significant difference was not found between REST and PDB group, it was a good experience to learn how to deal with the functional images and thinking the principle behind, since the functional image is different from the normal MR image, it usually incorporates with different type of stimulation to achieve the desire condition for studying the human brain, requiring not only the knowledge of physics and engineering, but also the knowledge of biology and medicine.

In this study, the brain perfusion and other arterial parameters were obtained and quantified from normocapnia and hypocapnia subjects, and the perfusion was supposed to be lower in hypocapnia than the one in normocapnia, however, the results showed that there was no significant difference even if the value of $P_{ET}CO_2$ decreases significantly. To explain this phenomenon, the only reason was the subjects did not achieve well the breathing task if every processing step was done correctly. Also, some of the subjects presented a high perfusion in occipital lobe during the PDB acquisition, it could happen if the abundant visual activation during imaging, since the breathing task was accomplished by displaying the instruction on screen, and the subjects probably over concentrated on the screen, and therefore the high perfusion.

On the other hand, different calibration methods were tested successfully in this work, having a significant difference between the methods used. Especially in the manner of saturation recovery with 100% saturation efficiency using reference tissue-based method, it impacted the value very much because of the high equilibrium magnetisation of the arterial blood, resulting an underestimation of absolute CBF. However, the calibration methods tested in this work, had no impact on the difference between the REST and PDB group, any significant difference was not found between the result of both conditions from all the calibration methods. The most reasonable manner were the voxel-wise methods, reference tissue GM and WM methods, since the absolute CBF values of these methods were observed in the range of 40 – 60 ml/100g/min, which was in the agreement with the previous studies (Chappell et al., 2010;

Sousa et al., 2013). However, more kind of calibration and their combination should be tested in order to have a comprehensive insight.

REFERENCES

Aherne EA, Koktzoglou I, Lind BB, Edelman RR. Dynamic quantitative nonenhanced magnetic resonance angiographyof the abdominal aorta and lower extremities using cine fast-interrupted steady-state in combination with arterial spin labeling: a feasibility study. J Cardiovasc Magn Reson. 2019 Sep 2;21(1):55.

Alsaedi A, Thomas D, Bisdas S, Golay X. Overview and Critical Appraisal of Arterial Spin Labelling Technique in Brain Perfusion Imaging. Contrast Media Mol Imaging. 2018 May 8;2018:5360375.

Birn RM, Smith MA., Jones TB, Bandettini PA, 2008. The respiration response function: the temporal dynamics of fMRI signal fluctuations related to changes in respiration. NeuroImage 40, 644–654.

Bokkers RP, van Laar PJ, van de Ven KC, Kapelle LJ, Klijn CJ, Hendrikse J. Arterial spin-labeling MR imaging measurements of timing parameters in patients with a carotid artery occlusion. AJNR Am J Neuroradiol. 2008 Oct;29(9):1698-703

Bright MG, Bulte DP, Jezzard P, Duyn JH. Characterization of regional heterogeneity in cerebrovascularreactivity dynamics using novel hypocapnia task and BOLD fMRI. Neuroimage. 2009 Oct 15;48(1):166-75.

Brown RW, Cheng YCN, Haacke EM, Tompson MR, Venkatesan R. Magnetic Resonance Imaging: Physical Principles and Sequences Design. Second Edition. John Wiley & Sons, Inc. 2014

Buxton RB, Frank LR, Wong EC, Siewert B, Warach S, Edelman RR. A general kinetic model for quantitative perfusion imaging with arterial spin labeling. Magn Reson Med. 1998 Sep;40(3):383-96.

Buxton RB. Introduction to Functional Magnetic Resonance Imaging: Principle and Techniques. Second Edition. Cambridge University Press. 2009

Chappell M, Groves R, Whitcher B, Woolrich W. Variational Bayesian inference for a nonlinear forward model. IEEE Transactions on Signal Processing (2009), 57(1), 223-236.

Chappell M, MacIntosh B, Okell T. Introduction to Perfusion Quantification using Arterial Spin Labeling. Oxford University Press 2018.

Chappell MA, MacIntosh BJ, Donahue MJ, Günther M, Jezzard P, Woolrich MW. Separation of macrovascular signal in multi-inversion time arterial spin labelling MRI. Magn Reson Med. 2010 May;63(5):1357-65. doi: 10.1002/mrm.22320.

Chen JJ, Pike GB. BOLD-specific cerebral blood volume and blood flow changes during neuronal activation in humans. NMR Biomed. 2009 Dec;22(10):1054-62.

Chen JJ, Pike GB. MRI measurement of the BOLD-specific flow-volume relationship during hypercapnia and hypocapnia in humans. Neuroimage. 2010 Nov 1;53(2):383-91.

Cipolla MJ. The Cerebral Circulation. Colloquium Series on Integrated Systems Physiology: From Molecule to Function (2009).

Coverdale NS, Gati JS, Opalevych O, Perrotta A, Shoemaker JK. Cerebral blood flow velocity underestimates cerebral blood flowduring modest hypercapnia and hypocapnia. J Appl Physiol (1985). 2014 Nov 15;117(10):1090-6.

Derdeyn CP, Videen TO, Yundt KD, Fritsch SM, Carpenter DA, Grubb RL, Powers WJ. Variability of cerebral blood volume and oxygen extraction: stages of cerebral haemodynamic impairment revisited. Brain. 2002 Mar;125(Pt 3):595-607.

Donahue MJ, Achten E, Cogswell PM, De Leeuw FE, Derdeyn CP, Dijkhuizen RM, Fan AP, Ghaznawi R, Heit JJ, Ikram MA, Jezzard P, Jordan LC, Jouvent E, Knutsson L, Leigh R, Liebeskind DS, Lin W, Okell TW, Qureshi AI, Stagg CJ, van Osch MJ, van Zijl PC, Watchmaker JM, Wintermark M, Wu O, Zaharchuk G, Zhou J, Hendrikse J. Consensus statement on current and emerging methods for the diagnosis and evaluation of cerebrovascular disease. J Cereb Blood Flow Metab. 2018 Sep;38(9):1391-1417.

Donahue MJ, Faraco CC, Strother MK, Chappell MA, Rane S, Dethrage LM, Hendrikse J, Siero JC. Bolus arrival time and cerebral blood flow responses to hypercarbia. J Cereb Blood Flow Metab. 2014 Jul;34(7):1243-52.

Folkman J. Angiogenesis in cancer, vascular, rheumatoid and other disease. Nat Med. 1995 Jan;1(1):27-31.

Francis ST, Bowtell R, Gowland PA. Modeling and optimization of Look-Locker spin labeling for measuring perfusion and transit time changes in activation studies taking into account arterial blood volume. Magn Reson Med. 2008 Feb;59(2):316-25.

Gomes G. Non-invasive quantitative imaging of brain perfusion in hypocapnia by ASL MRI. Master degree thesis in biomedical engineering (2015). Instituto Superior Técnico, University of Lisbon.

Groves AR, Chappell MA, Woolrich MW, Combined Spatial and Non-Spatial Prior for Inference on MRI Time-Series, NeuroImage 45(3) 795-809, 2009.

Grubb RL Jr, Raichle ME, Eichling JO, Ter-Pogossian MM. The effects of changes in PaCO2 on cerebral blood volume, blood flow, and vascular mean transit time. Stroke. 1974 Sep-Oct;5(5):630-9.

Günther M (2013). Perfusion Imaging. Journal of Magnetic Resonance Imaging: JMRI, 279, 269-279.

Hansen-Smith F, Egginton S, Zhou AL, Hudlicka O. Growth of arterioles precedes that of capillaries in stretch-induced angiogenesis in skeletal muscle. Microvasc Res. 2001 Jul;62(1):1-14.

Hendrikse J, Lu H, van der Grond J, Van Zijl PC, Golay X. Measurements of cerebral perfusion and arterial hemodynamics during visual stimulation using TURBO-TILT. Magn Reson Med. 2003 Aug;50(2):429-33.

Herscovitch P, Raichle ME. What is the correct value for the brain--blood partition coefficient for water? J Cereb Blood Flow Metab. 1985 Mar;5(1):65-9.

Ho YC[1], Petersen ET, Zimine I, Golay X. Similarities and differences in arterial responses to hypercapnia and visual stimulation. J Cereb Blood Flow Metab. 2011 Feb;31(2):560-71.

Hua J, Liu P, Kim T, Donahue M, Rane S, Chen JJ, Qin Q, Kim SG. MRI techniques to measure arterial and venous cerebral blood volume. Neuroimage. 2019 Feb 15;187:17-31.

Hua J, Qin Q, Donahue MJ, Zhou J, Pekar JJ, van Zijl PC. Inflow-based vascular-space-occupancy (iVASO) MRI. Magn Reson Med. 2011 Jul;66(1):40-56.

Hua J, Stevens R, Donahue MJ, Huang AJ, Pekar J, Van Zijl PCM. Cerebral blood volume changes in arterial and post-arterial compartments and their relationship with cerebral blood flow alteration during brief breath-hoding and visual stimulation in human brain. In: Proc. 18th Annual Metting ISMRM (2010), Stockholm, Sweden, p. 1127.

Ito H, Kanno I, Ibaraki M, Hatazawa J, Miura S. Changes in human cerebral blood flow and cerebral blood volume during hypercapnia and hypocapnia measured by positron emission tomography. J Cereb Blood Flow Metab. 2003 Jun;23(6):665-70.

Jenkinson M, Beckmann CF, Behrens TE, Woolrich MW, Smith SM. FSL. NeuroImage, 62:782-90, 2012

Jezzard P, Chappell MA, Okell TW. Arterial spin labeling for the measurement of cerebral perfusion and angiography. J Cereb Blood Flow Metab. 2018 Apr;38(4):603-626.

Kida I, Rothman DL, Hyder F. Dynamics of changes in blood flow, volume, and oxygenation: implications for dynamic functional magnetic resonance imaging calibration. J Cereb Blood Flow Metab. 2007 Apr;27(4):690-6.

Krainik A, Hund-Georgiadis M, Zysset S, von Cramon DY, 2005. Regional impairment of cerebrovascular reactivity and BOLD signal in adults after stroke. Stroke 36, 1146–1152.

Law M, Yang S, Babb JS, Knopp EA, Golfinos JG, Zagzag D, Johnson G. Comparison of cerebral blood volume and vascular permeability from dynamic susceptibility contrast-enhanced perfusion MR imaging with glioma grade. AJNR Am J Neuroradiol. 2004 May;25(5):746-55.

Lee Y, Kim T. Assessment of hypertensive cerebrovascular alterations with multiband Look-Locker arterial spin labeling. J Magn Reson Imaging. 2018 Mar;47(3):663-672.

Liang ZP, Lauterbur PC. Principle of Magneric Resonance Imaging: A Signal Processing Perspective. The Institute of Electrical and Electronics Engineers, Inc., New York. 2000.

Liu P, De Vis JB, Lu H. Cerebrovascular reactivity (CVR) MRI with CO2 challenge: A technical review. Neuroimage. 2019 Feb 15;187:104-115.

Luh WM[1], Wong EC, Bandettini PA, Hyde JS. QUIPSS II with thin-slice TI1 periodic saturation:a method for improving accuracy of quantitative perfusion imaging using pulsedarterial spin labeling. Magn Reson Med. 1999 Jun;41(6):1246-54.

MacIntosh BJ, Filippini N, Chappell MA, Woolrich MW, Mackay CE, Jezzard P. Assessment of arterial arrival times derived from multiple inversion time pulsed arterial spin labeling MRI. Magn Reson Med. 2010 Mar;63(3):641-7

MacIntosh BJ, Pattinson KT, Gallichan D, Ahmad I, Miller KL, Feinberg DA, Wise RG, Jezzard P. Measuring the effects of remifentanil on cerebral blood flow and arterial arrival time using 3D GRASE MRI with pulsed arterial spin labelling. J Cereb Blood Flow Metab. 2008 Aug;28(8):1514-22.

Mäkiranta MJ, Ruohonen J, Suominen K, Sonkajärvi E, Salomäki T, Kiviniemi V, Seppänen T, Alahuhta S, Jäntti V, Tervonen O. BOLD-contrast functional MRI signal changes related to intermittent rhythmic delta activity in EEG during voluntary hyperventilation-simultaneous EEG and fMRI study. NeuroImage. 2004 22, 222–231.
Nöth U, Meadows GE, Kotajima F, Deichmann R, Corfield DR, Turner R. Cerebral vascular response to hypercapnia: determination with perfusion MRI at 1.5 and 3.0 Tesla using a pulsed arterial spin labeling technique. J Magn Reson Imaging. 2006 Dec;24(6):1229-35.

Pindzola RR, Balzer JR, Nemoto EM, Goldstein S, Yonas H. Cerebrovascular reserve in patients with carotid occlusive disease assessed by stable xenon-enhanced ct cerebral blood flow and transcranial Doppler. Stroke. 2001 Aug;32(8):1811-7.

Pinto J. Spatiotemporal dynamics of CBF and BOLD fMRI responses to breath-hold challenges. Master degree thesis in biomedical engineering (2012), Instituto Superior Técnico, University of Lisbon

Posse S, Olthoff U, Weckesser M, Jäncke L, Müller-Gärtner HW, Dager SR. Regional dynamic signal changes during controlled hyperventilation assessed with blood oxygen level-dependent functional MR imaging. AJNR Am J Neuroradiol. 1997 Oct;18(9):1763-70.

Rostrup E, Knudsen GM, Law I, Holm S, Larsson HB, Paulson OB. The relationship between cerebral blood flow and volume in humans. Neuroimage. 2005 Jan 1;24(1):1-11.

Smith SM, Jenkinson M, Woolrich MW, Beckmann CF, Behrens TEJ, Johansen-Berg H, Bannister PR, De Luca M, Drobnjak I, Flitney DE, Niazy R, Saunders J, Vickers J, Zhang Y, De Stefano N, Brady JM, and Matthews PM. Advances in functional and structural MR image analysis and implementation as FSL. NeuroImage, 23(S1):208-19, 2004

Smith SM, Nichols TE. Threshold-free cluster enhancement: addressing problems of smoothing, threshold dependence and localisation in clusterinference. Neuroimage. 2009 Jan 1;44(1):83-98.

Sousa I, Vilela P, Figueiredo P. Reproducibility of hypocapnic cerebrovascular reactivity measurements using BOLD fMRI in combination with a paced deep breathing task. Neuroimage. 2014 Sep;98:31-41.

Sousa I, Vilela P, Figueiredo P. Reproducibility of the quantification of arterial and tissue contributions in multiple postlabeling delay arterial spin labeling. J Magn Reson Imaging. 2014 Dec;40(6):1453-62.

Ssali T, Anazodo UC, Thiessen JD, Prato FS, St Lawrence K. A Noninvasive Method for Quantifying Cerebral Blood Flow by HybridPET/MRI. J Nucl Med. 2018 Aug;59(8):1329-1334.

Verbree J, Bronzwaer AS, Ghariq E, Versluis MJ, Daemen MJ, van Buchem MA, Dahan A, van Lieshout JJ, van Osch MJ. Assessment of middle cerebral artery diameter during hypocapniaand hypercapnia in humans using ultra-high-field MRI. J Appl Physiol (1985). 2014 Nov 15;117(10):1084-9.

Vogt KM, Ibinson, JW Schmalbrock P, Small RH, 2011. Comparison between end-tidal CO and respiration volume per time for detecting BOLD signal fluctuations during paced hyperventilation. Magn. Reson. Imaging 29, 1186–1194.

Weckesser M, Posse S, Olthoff U, Kemna L, Dager S, Muller-Gartner HW. Functional imaging of the visual cortex with bold-contrast MRI: hyperventilation decreases signal response. Magn. Reson. Med. 1999. 41, 213–216.

Williams DS, Detre JA, Leigh JS, Koretsky AP. Magnetic resonance imaging of perfusion using spin inversion of arterial water. Proc Natl Acad Sci USA 1992; 89:212-216.

Winkler AM, Ridgway GR, Webster MA, Smith SM, Nichols TE. Permutation inference for the general linear model. Neuroimage. 2014 May 15;92:381-97.

Wirestam R, Engvall C, Ryding E, Holtas S, Stahlberg F, Reinstrup P. Changes in cerebral perfusion detected by dynamic susceptibility contrast magnetic resonance imaging: normal volunteers examined during normal breathing and hyperventilation. J. Biomedical Science and Engineering, 2009, 2, 210-215

Wong EC, Buxton RB, Frank LR. Implementation of quantitative perfusion imaging techniques for functional brain mapping using pulsed arterial spin labeling. NMR in Biomed 1997; 10:237-249.

Woolrich WM, Jbabdi S, Patenaude B, Chappell M, Makni S, Behrens T, Beckmann C, Jenkinson M, Smith SM. Bayesian analysis of neuroimaging data in FSL. NeuroImage, 45:S173-86, 2009

Wu G[1], Luo F, Li Z, Zhao X, Li SJ. Transient relationships among BOLD, CBV, and CBF changes in rat brain as detected by functional MRI. Magn Reson Med. 2002 Dec;48(6):987-93.

Yang Y, Engelien W, Xu S, Gu H, Silbersweig DA, Stern E. Transit time, trailing time, and cerebral blood flow during brain activation: measurement using multislice, pulsed spin-labeling perfusion imaging. Magn Reson Med. 2000 Nov;44(5):680-5.

Yonas H, Darby JM, Marks EC, Durham SR, Maxwell C. CBF measured by Xe-CT: approach to analysis and normal values. J Cereb Blood Flow Metab. 1991 Sep;11(5):716-25.

APPENDIX

APPENDIX

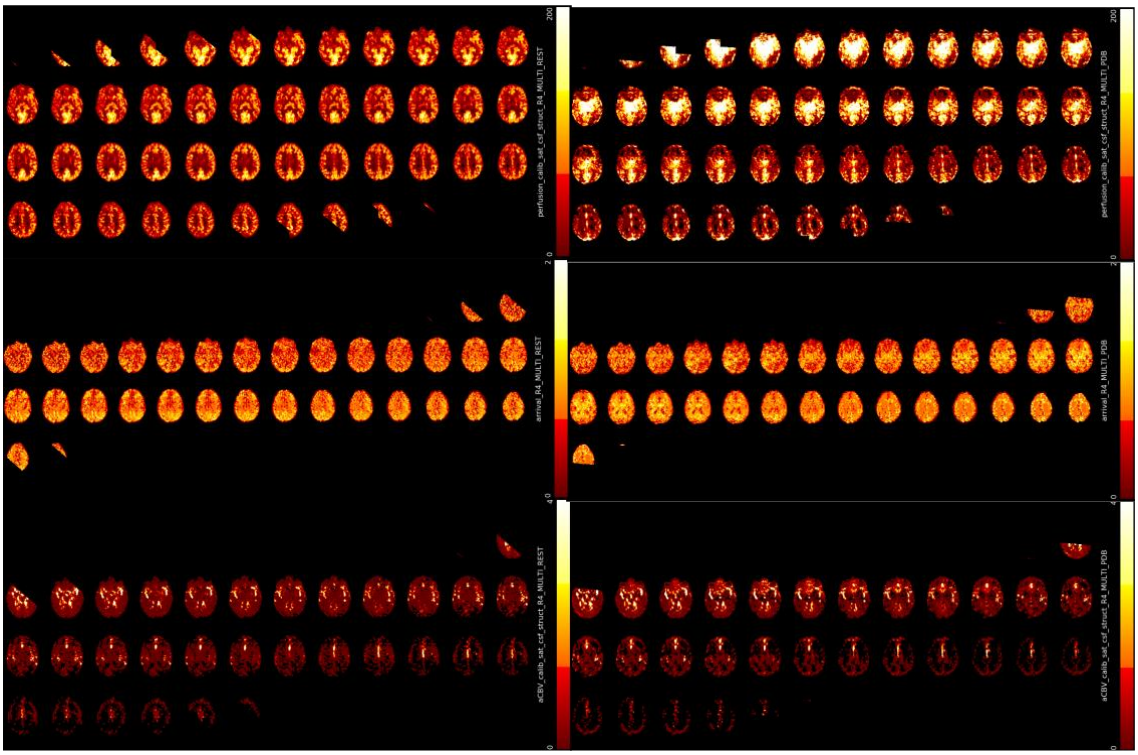

Appendix 1: CBF (upper row), ATT (middle row), aBV (lower row) map of S1 in during REST (left column) and PDB (right column).

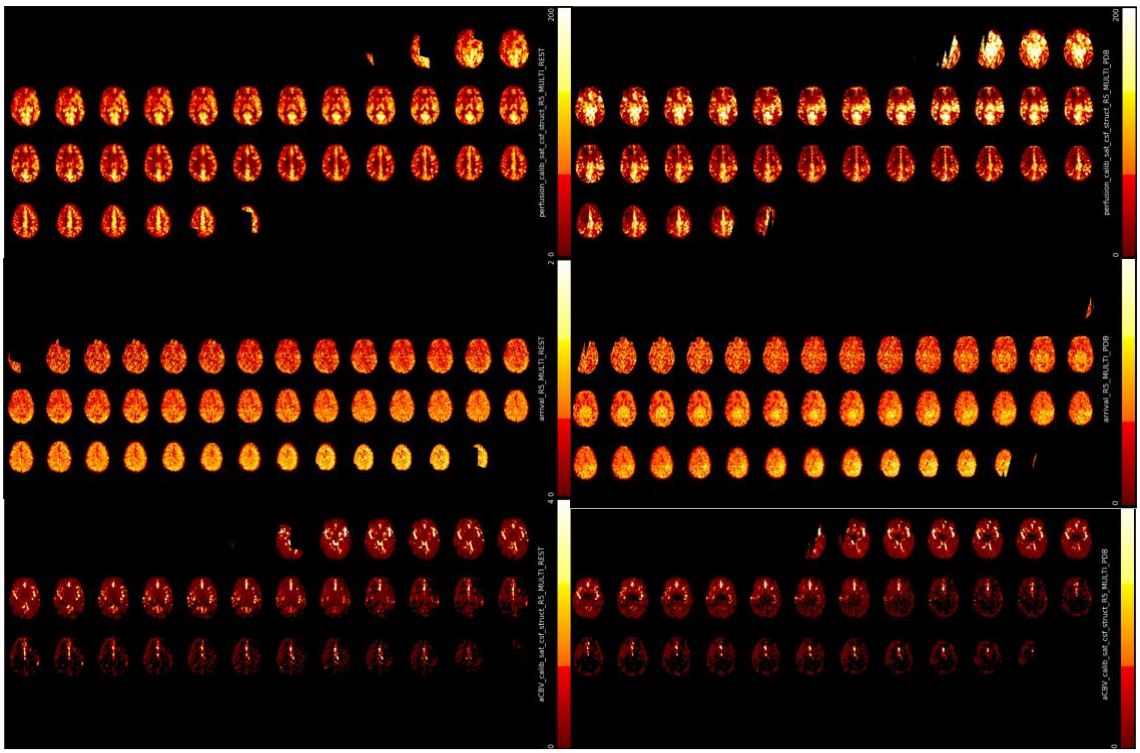

Appendix 2: CBF (upper row), ATT (middle row), aBV (lower row) map of S2 in during REST (left column) and PDB (right column).

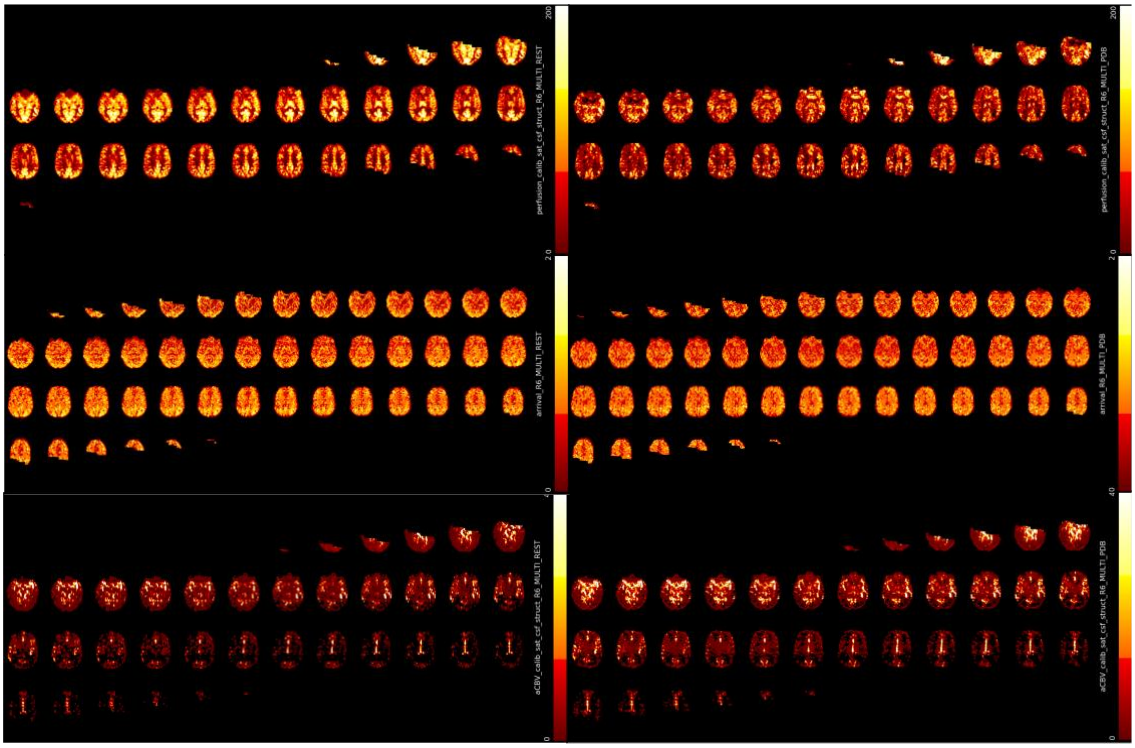

Appendix 3: CBF (upper row), ATT (middle row), aBV (lower row) map of S3 in during REST (left column) and PDB (right column).

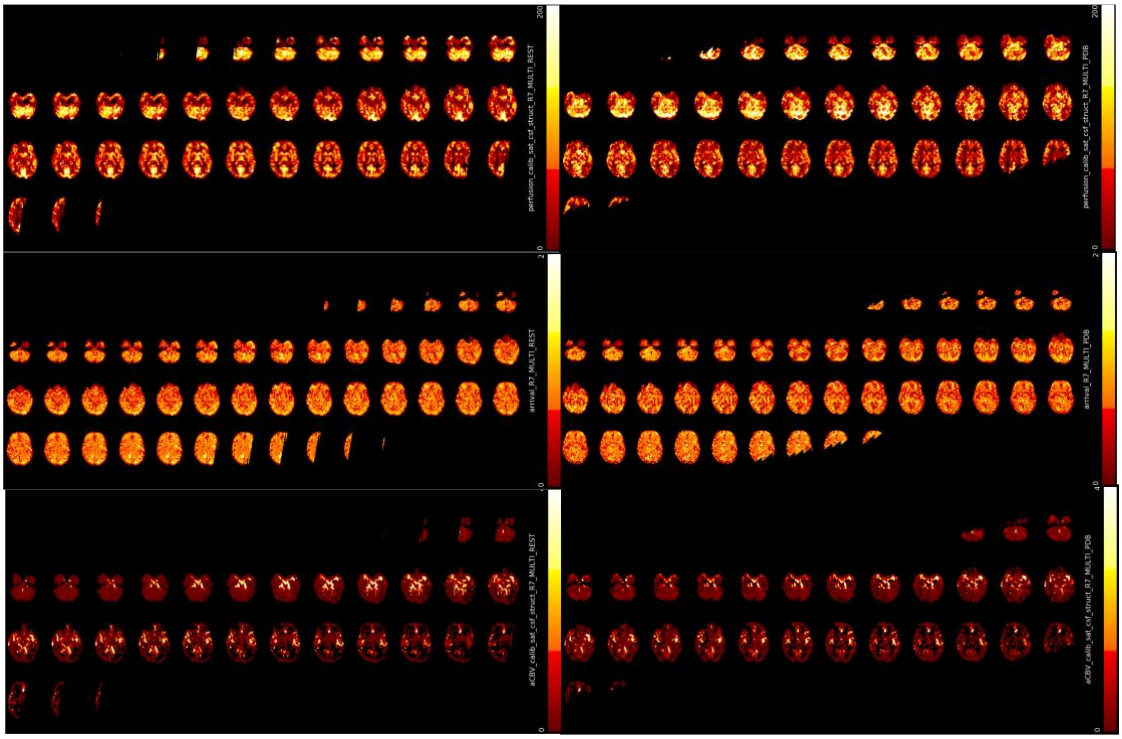

Appendix 4: CBF (upper row), ATT (middle row), aBV (lower row) map of S4 in during REST (left column) and PDB (right column).

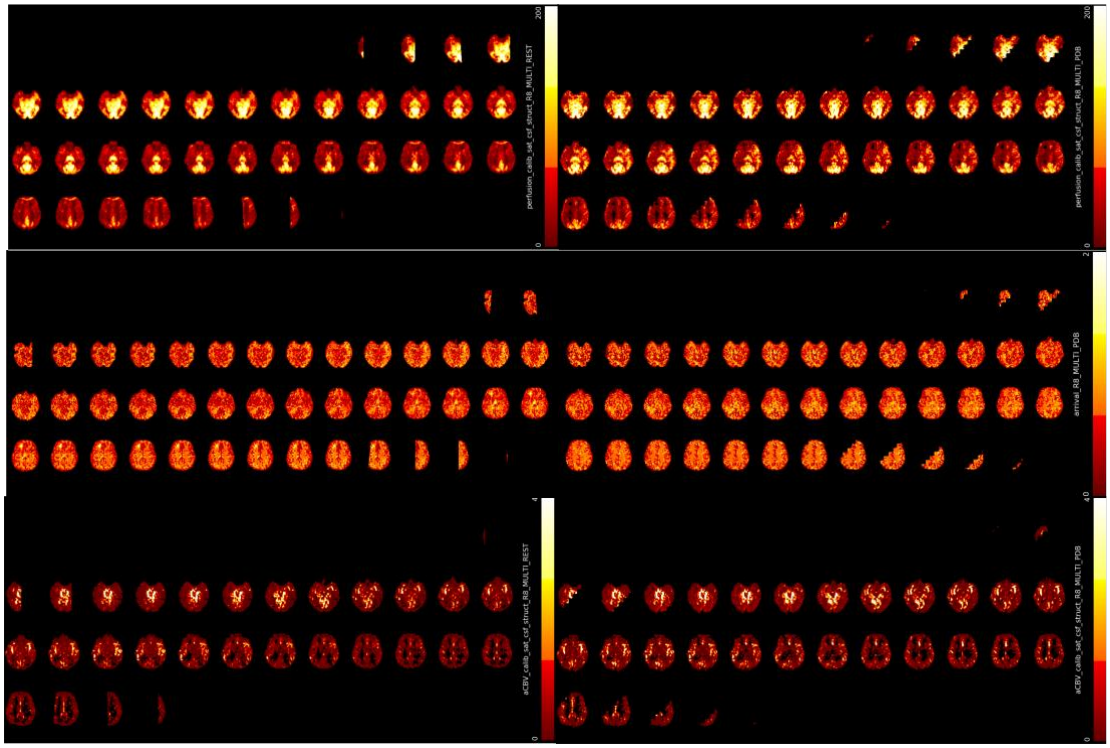

Appendix 5: CBF (upper row), ATT (middle row), aBV (lower row) map of S5 in during REST (left column) and PDB (right column).

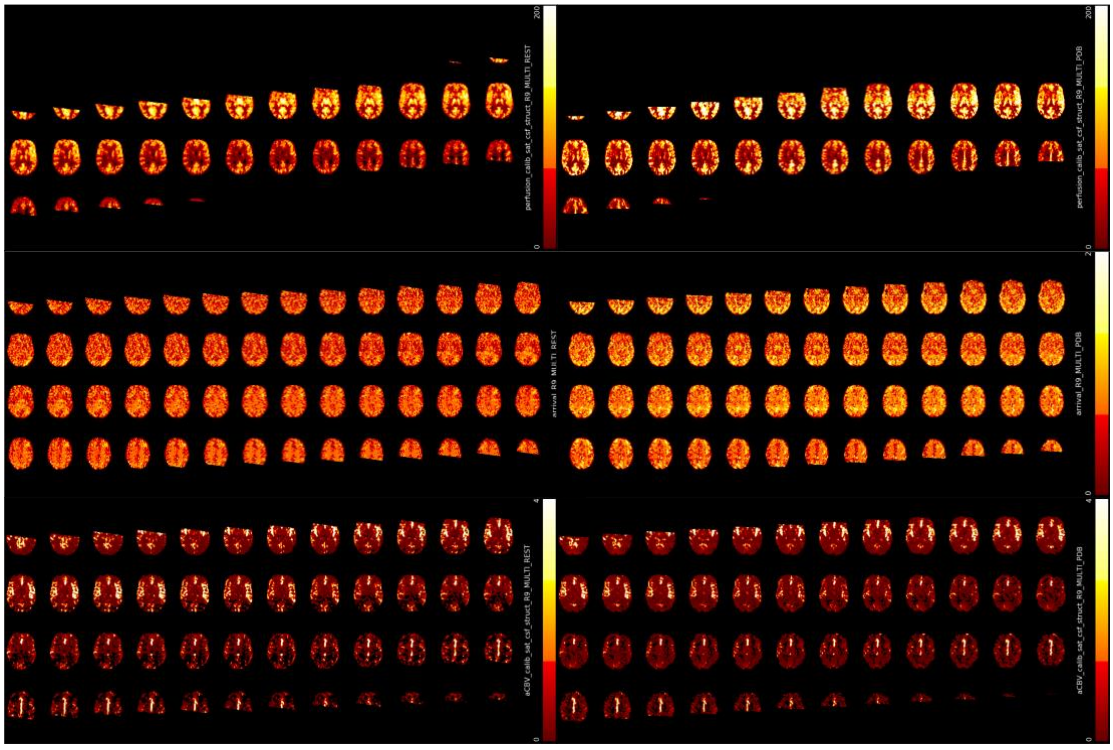

Appendix 6: CBF (upper row), ATT (middle row), aBV (lower row) map of S6 in during REST (left column) and PDB (right column).

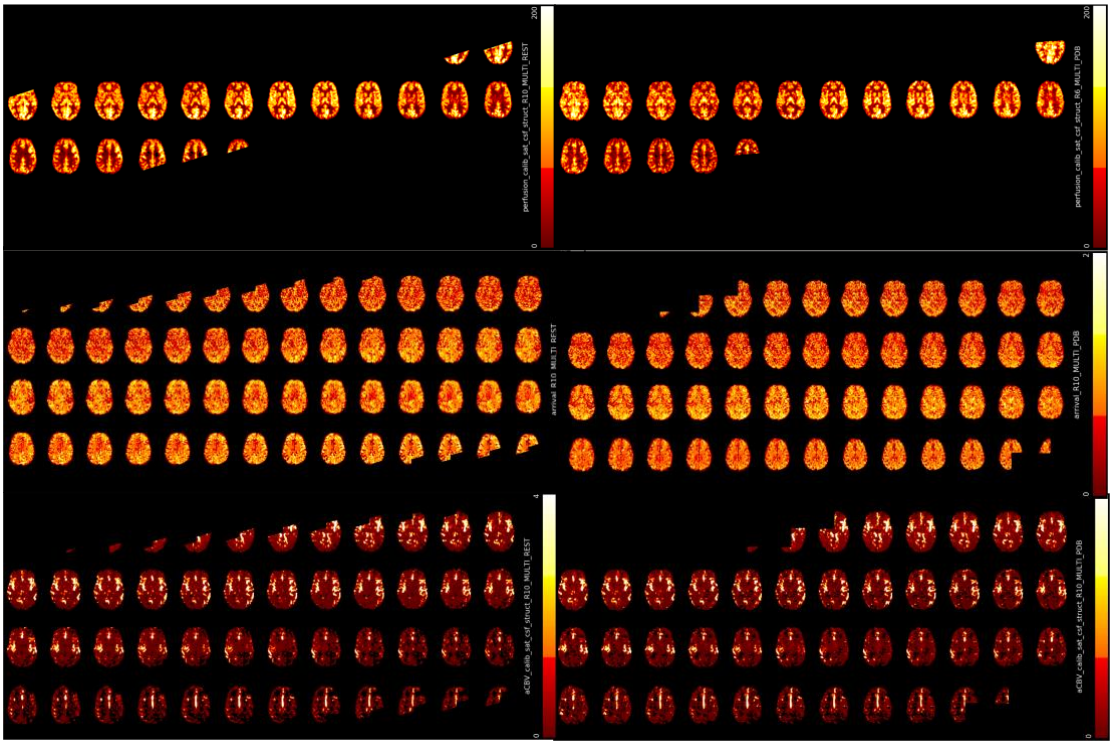

Appendix 7: CBF (upper row), ATT (middle row), aBV (lower row) map of S7 in during REST (left column) and PDB (right column).

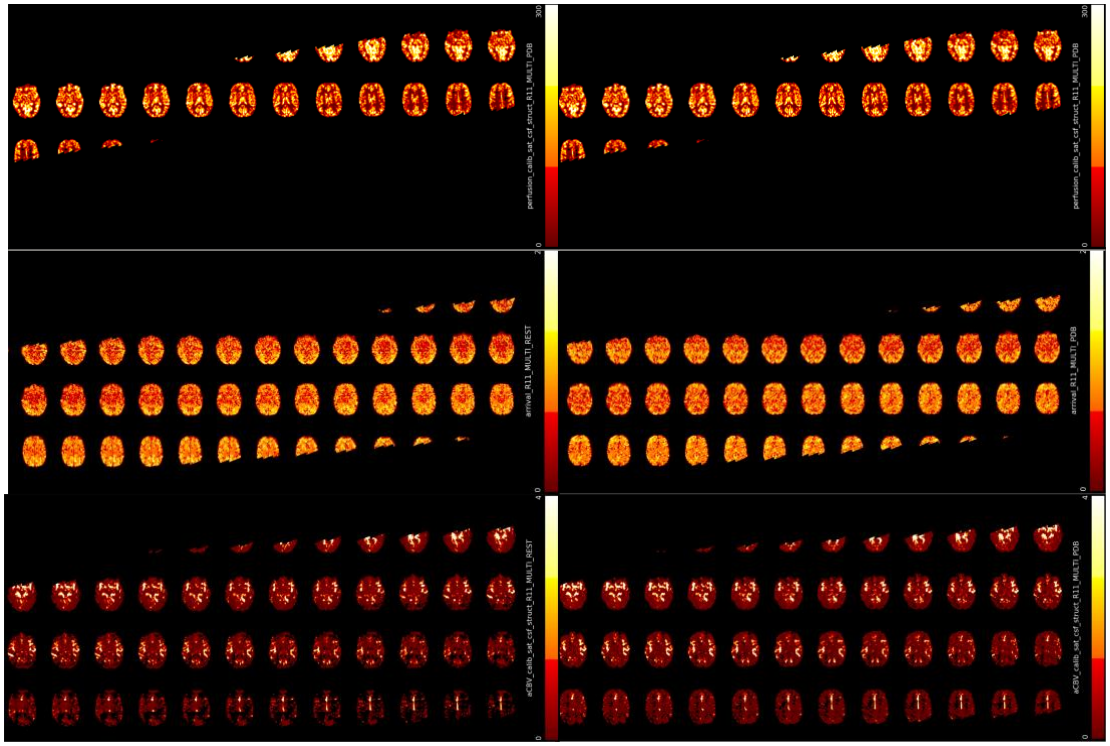

Appendix 8: CBF (upper row), ATT (middle row), aBV (lower row) map of S8 in during REST (left column) and PDB (right column).

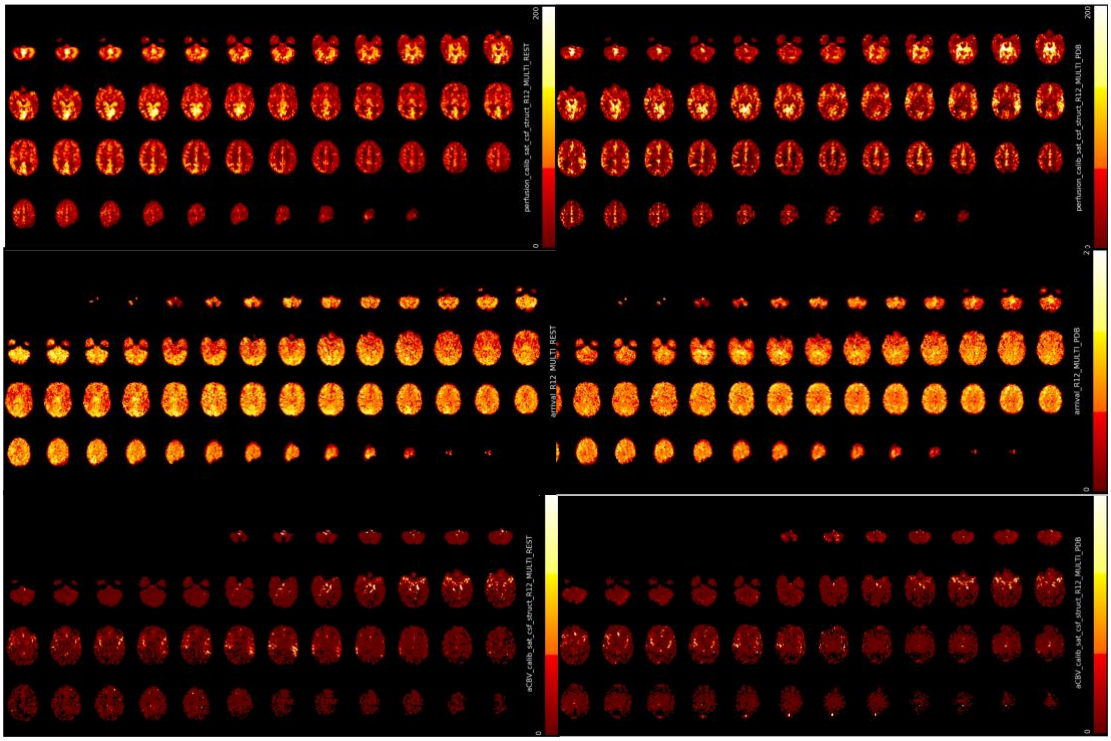

Appendix 9: CBF (upper row), ATT (middle row), aBV (lower row) map of S9 in during REST (left column) and PDB (right column).

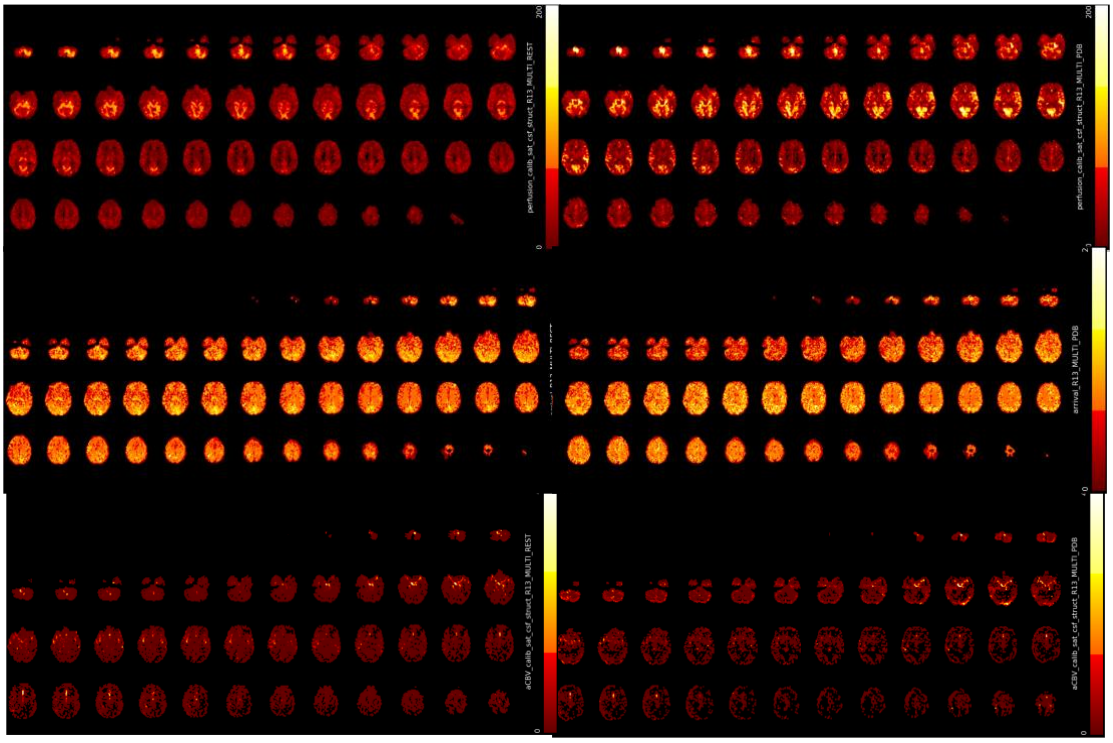

Appendix 10: CBF (upper row), ATT (middle row), aBV (lower row) map of S10 in during REST (left column) and PDB (right column).

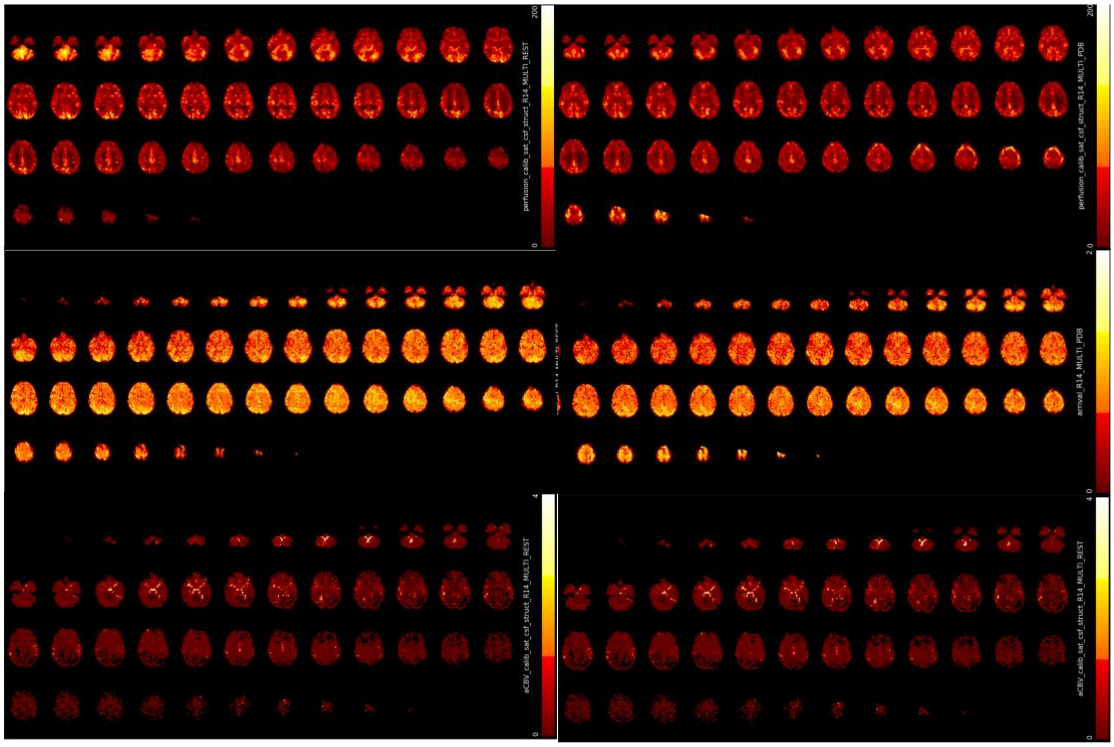

Appendix 11: CBF (upper row), ATT (middle row), aBV (lower row) map of S11 in during REST (left column) and PDB (right column).

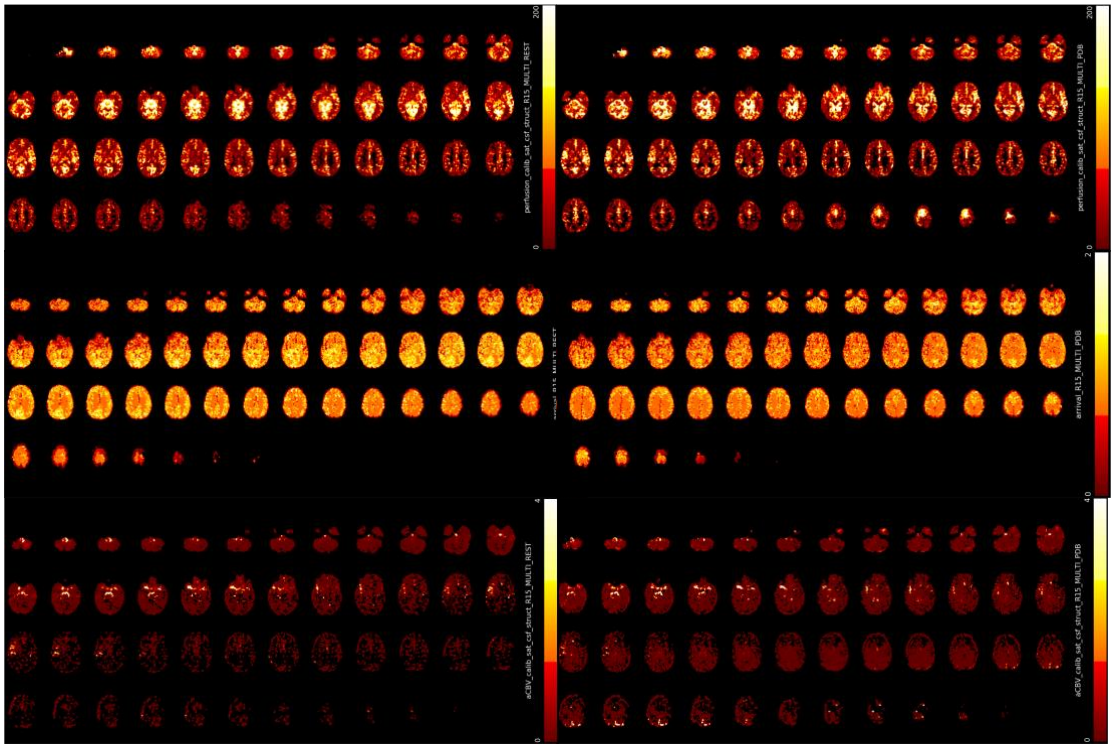

Appendix 12: CBF (upper row), ATT (middle row), aBV (lower row) map of S12 in during REST (left column) and PDB (right column).